

Doctoral Thesis

**Search for electromagnetic
counterparts to neutrinos and
gravitational waves**

**Searching for sources of astrophysical neutrinos and gravitational
waves**

Robert Stein

May 5, 2021

Humboldt Universitaet Berlin

Disclaimer

You can edit this page to suit your needs. For instance, here we have a no copyright statement, a colophon and some other information. This page is based on the corresponding page of Ken Arroyo Ohori's thesis, with minimal changes.

No copyright

©⑧ This book is released into the public domain using the CC0 code. To the extent possible under law, I waive all copyright and related or neighbouring rights to this work. To view a copy of the CC0 code, visit:

<http://creativecommons.org/publicdomain/zero/1.0/>

Colophon

This document was typeset with the help of **KOMA-Script** and **L^AT_EX** using the **kaobook** class.

The source code of this thesis is available at:

<https://github.com/robertdstein/kaobook>,

while the scripts used to generate the plots is available at:

https://github.com/robertdstein/thesis_code

The template is a modification of the open-source kaobook class, available at:

<https://github.com/fmarotta/kaobook>

Publisher

First printed in Feb 2021 by Humboldt Universitaet Berlin

A neutrino is not a big thing to be hit by.
In fact it's hard to think of anything much smaller by which
one could reasonably hope to be hit. And it's not as if being
hit by neutrinos was in itself a particularly unusual event for
something the size of the Earth. Far from it. It would be an
unusual nanosecond in which the Earth was not hit by
several billion passing neutrinos.

–The Hitchhiker's Guide to The Galaxy

Preface

I am of the opinion that every \LaTeX geek, at least once during his life, feels the need to create his or her own class: this is what happened to me and here is the result, which, however, should be seen as a work still in progress. Actually, this class is not completely original, but it is a blend of all the best ideas that I have found in a number of guides, tutorials, blogs and tex.stackexchange.com posts. In particular, the main ideas come from two sources:

- ▶ Ken Arroyo Ohori's [Doctoral Thesis](#), which served, with the author's permission, as a backbone for the implementation of this class;
- ▶ The [Tufte-Latex Class](#), which was a model for the style.

The first chapter of this book is introductory and covers the most essential features of the class. Next, there is a bunch of chapters devoted to all the commands and environments that you may use in writing a book; in particular, it will be explained how to add notes, figures and tables, and references. The second part deals with the page layout and design, as well as additional features like coloured boxes and theorem environments.

I started writing this class as an experiment, and as such it should be regarded. Since it has always been intended for my personal use, it may not be perfect but I find it quite satisfactory for the use I want to make of it. I share this work in the hope that someone might find here the inspiration for writing his or her own class.

Federico Marotta

Contents

Preface	v
Contents	vi
AN INTRODUCTION TO MULTI-MESSENGER ASTRONOMY	1
NEUTRINO ASTRONOMY WITH ICECUBE	3
1 Statistical Analysis in IceCube	5
1.1 Hypothesis Testing	6
1.2 Null Hypothesis and Background Modelling	7
1.3 Signal Hypothesis	9
1.4 Likelihoods and Wilk's Theorem	13
1.5 Pseudo-trials, P-values and trial corrections	14
1.6 Sensitivities, Discovery Potentials and Upper Limits	16
1.7 Stacking Multiple Sources	19
1.8 Combining seasons	20
1.9 Cluster-search algorithm	20
1.10 Fitting the relative source weights	22
1.11 Flarestack in practice	22
2 Stacking Analyses with IceCube	25
2.1 Tidal Disruption Events	25
2.2 AT2018cow and FBOTs	33
2.3 Robustness of Limits	35
OPTICAL FOLLOW-UP WITH ZTF	37
CONCLUSION	39
APPENDIX	41
A TDE Catalogue Results	43
Bibliography	47
Alphabetical Index	49

List of Figures

1.2	Event rate as a function of $\sin(\delta)$	8
1.1	Rolling average of final-level event rate during detector uptime.	8
1.3	Declination-normalised event rate as a function of azimuth.	9
1.4	Background energy proxy distribution, normalised in bins of $\sin(\delta)$	9
1.5	Background energy proxy distribution, normalised in bins of azimuth.	9
1.6	Left: Declination-normalised MC rate as a function of azimuth. Right: Ratio of declination-normalised Signal and Background PDFs.	12
1.7	Left: Energy proxy distribution as a function of $\sin(\delta)$, for various signal hypotheses. Right: Ratio of declination-normalised Signal and Background PDFs.	13
1.8	Background TS distribution for the standard Point Source Likelihood (Equation 1.17).	15
1.9	Background TS distribution for a Point Source Likelihood without an energy term.	15
1.10	Signal TS distribution for the standard Point Source Likelihood (Equation 1.17), with ≈ 3 injected neutrinos.	16
1.11	Signal TS distribution for the Point Source Likelihood without an energy term, with ≈ 3 injected neutrinos.	16
1.12	Sensitivity for the standard Point Source Likelihood (Equation 1.17), using the background TS distribution from Figure 1.8.	17
1.13	Sensitivity for the Point Source Likelihood without an energy term, using the background TS distribution from Figure 1.9.	17
1.14	5σ Discovery Potential for the standard Point Source Likelihood (Equation 1.17), using background TS distribution from Figure 1.8.	17
1.15	5σ Discovery Potential for the Point Source Likelihood without an energy term, using background TS distribution from Figure 1.9.	17
1.16	Effective area as a function of neutrino energy and declination.	18
1.17	Sensitivity and Discovery potential as a function of declination for an E^{-2} spectrum.	18
1.18	Visualisation of a spatial PDF.	20
1.19	Visualisation of an energy proxy PDF.	20
1.20	Visualisation of the cluster search algorithm.	21
1.21	Estimated 5σ Discovery Potential for AT2018cow as a function of flare length, given in units of total fluence for an E^{-2} spectrum over the 130 day search window.	21
2.1	Limits on the neutrino fluence for each catalogue.	29
2.2	Limits on the per-source neutrino emission for each catalogue.	30
2.3	Limits on the contribution of jetted and non-jetted TDEs to the diffuse neutrino flux.	31
2.4	Limits on the contribution of jetted and non-jetted TDEs to the diffuse neutrino flux, under the assumption of a source evolution proportional to the Star Formation Rate.	32
2.5	Limits on neutrino emission from AT2018cow, as a function of spectral index.	34
2.6	Limits on neutrino emission from FBOTs, using the limits from AT2018cow under the assumption of neutrino standard candles.	34

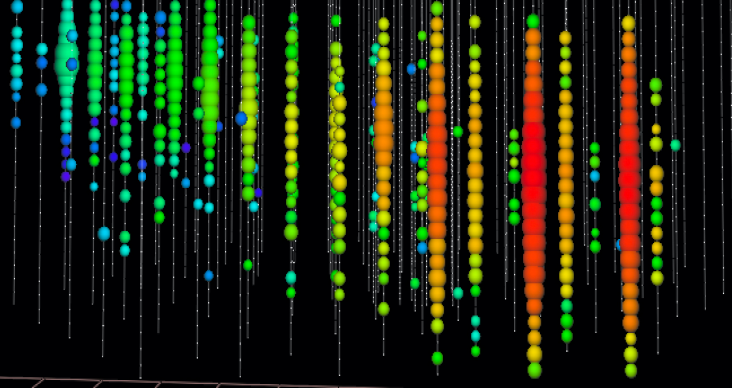
2.7 Sensitivity of the Point Source Likelihood for a point source as a function of energy.	36
--	----

List of Tables

2.1 Summary of the four TDE catalogues..	27
2.2 Summary of results for the four TDE catalogues. For each, an independent stacking analysis was performed. The catalogues covered sources from May 2008 to October 2017, matching the IceCube data-taking period.	28
2.3 Summary of the five individual TDEs for which the temporal-cluster-search method was applied. All but AT2018cow were included in the stacking analysis.	32
A.1 Summary of the Jetted TDE catalogue.	43
A.2 Summary of the Golden TDE catalogue.	44
A.3 Summary of the Silver TDE catalogue.	44
A.4 Summary of the Obscured TDE catalogue.	45

**AN INTRODUCTION TO
MULTI-MESSENGER ASTRONOMY**

NEUTRINO ASTRONOMY WITH ICECUBE



1 Statistical Analysis in IceCube

“ Every experiment may be said to exist only in order to give the facts a chance of disproving the null hypothesis. ”

Ronald Fischer, *The Design of Experiments*, 1935

As a field, Neutrino Astronomy is still very much in its infancy. While most branches of astronomy are focussed on characterising the properties of astrophysical objects, neutrino astronomy primarily seeks to just identify such objects in the first place. Given the characteristic signal-to-noise of neutrino detectors, determined by their limited resolution and event rate with an enormous atmospheric background, a significant fraction of correlations in data will be due simply to background fluctuations. This statement applies both to clustering within the neutrino data, and to correlations between neutrinos and external data.

Neutrino astronomy is thus predominantly a process of statistical analysis, seeking both to identify correlations and to evaluate whether these are coincidental or physical. As introduced in Chapter ??, we have access to three key observables when performing this analysis with IceCube:

- ▶ **Event arrival time**, t , with nanosecond precision.
- ▶ **Reconstructed direction**, zenith (θ) and azimuth (ϕ), in local detector coordinates. This quantity has a significant uncertainty, which can also be estimated, providing an additional observable (σ). The reconstructed direction, in combination with the time, can be uniquely mapped to celestial coordinates Right Ascension (α) and Declination (δ).
- ▶ **Event energy proxy**, E_p . It can be converted through *unfolding* to give a probability distribution of true neutrino energies, but this requires certain assumptions about the underlying neutrino spectrum and retains typical uncertainties of factor 10.

This chapter outlines the process by which these observables are analysed, and correlations are established. A software designed to perform

1.1 Hypothesis Testing	6
1.2 Null Hypothesis and Background Modelling	7
1.3 Signal Hypothesis	9
1.4 Likelihoods and Wilk’s Theorem	13
1.5 Pseudo-trials, P-values and trial corrections	14
1.6 Sensitivities, Discovery Potentials and Upper Limits .	16
1.7 Stacking Multiple Sources .	19
1.8 Combining seasons	20
1.9 Cluster-search algorithm .	20
1.10 Fitting the relative source weights	22
1.11 Flarestack in practice	22

[1]: Stein et al. (2020), [icecube/flarestack](#)

such analysis, `flarestack`, was developed by the author to study correlations in IceCube data [1].

1.1 Hypothesis Testing

Neutrino Astronomy with IceCube uses a *Frequentist* approach to statistical inference, and in particular uses the method of *statistical hypothesis testing* to establish correlations. Statistical hypothesis testing begins with the definition of a particular hypothesis to test, \mathcal{H}_1 , and a null hypothesis, \mathcal{H}_0 , that would be expected in the absence of any correlation. Ultimately, we wish to determine which hypothesis better describes our data. Hypothesis testing adopts the default position that the null hypothesis describes the data, and evaluates whether this description can be disproven. We define a test statistic (TS) to quantify how well data is described, and define a threshold at which we would be confident in reaching a conclusion. If our test statistic exceeds this threshold, we *reject the null hypothesis*. This means we are confident that the null hypothesis does not describe our data. It does not necessarily follow that our signal hypothesis is correct, we can only say that it better describes our data than the null hypothesis. Conversely, if the TS does not exceed the threshold, we *do not reject the null hypothesis*. In this case, we are not confident that the null hypothesis does not describe our data. This does not mean that the signal hypothesis is wrong, but rather that we cannot be sure the null hypothesis is wrong.

Table 1.1: Hypothesis Testing

	not rejected	rejected
\mathcal{H}_0 true	✓	Type I
\mathcal{H}_0 false	Type II	✓

As illustrated in Table 1.1, there are two things that can go wrong with a hypothesis test. Type I error, or a false positive, occurs when we reject the null hypothesis although it is true. Type II error, or a false negative, occurs when we do not reject the null hypothesis even though it is false. By construction, every test must balance the risk of Type I and Type II errors, and both cannot be eliminated simultaneously. We typically construct our test by fixing a threshold for acceptable rate of Type I error. This Type I error rate is quantified by a *p-value*, defined as the probability of observing a result under the null hypothesis that is at least as significant as the one found. One common p-value threshold is 0.05, i.e. only accepting results with a probability $< 5\%$ to arise under the null hypothesis. The p-value can also be converted to a *significance*, equal to the number of standard deviations required for a one-sided Gaussian distribution to yield that p-value. A typical threshold for a discovery, common in particle physics, is 5σ . This corresponds to a p-value of less than 3×10^{-7} .

While the simplest hypothesis test is a binary case in which one well-defined hypothesis \mathcal{H}_1 is compared to the null hypothesis, the procedure is often generalised to cover multiple hypotheses, \mathcal{H}_i , which can be either discrete or continuous. We pick the hypothesis with the smallest p-value, and compare that to our null hypothesis.

1.2 Null Hypothesis and Background Modelling

For neutrino astronomy, the null hypothesis is that *events are distributed according to the background model*. At the stage of defining background models, IceCube-specific physics is added to the pure mathematical basis of hypothesis testing. As outlined in Chapter ??, IceCube data in the northern hemisphere is dominated by the *atmospheric neutrino background*, while events in the southern hemisphere are dominated by *atmospheric muon bundles*, and in both hemispheres the astrophysical neutrino component is subdominant. This astrophysical neutrino flux likely consists of components from multiple source classes, so there is in principle an additional *astrophysical background* for contributions not included in the signal hypothesis.

It is common in IceCube to take the simplifying assumption that *the data is sufficiently background-dominated to be used as a background model*. The motivation is twofold, it is firstly approximately true, but more importantly the colossal muon rate ($\sim 3\text{kHz}$) makes it very difficult to simulate the small fraction of muons which form a signal-like background for the southern hemisphere [2]. In the absence of any adequate simulated model for background in the southern hemisphere, we are forced to instead use a data-based model as a null hypothesis.

The simplification has a number of drawbacks, primarily that Probability Density Functions (PDFs) derived from data are necessarily coarser because the available statistics are limited. An alternative approach, used for the sample of northern through-going muons tracks in which there is negligible atmospheric muon background, is to use Monte-Carlo based modelling to construct a model for background [3]. This ultimately introduces the risk of data-MC disagreement, with uncertainties introduced for example with by atmospheric and astrophysical flux modelling. However, this is typically offset by the high-resolution PDFs which can be constructed using these much larger sample sizes.

In either case, distributions are then constructed for the background model \mathcal{B} . Using our observables, we can construct a composite background model consisting of a spatial, temporal and energy component:

$$\mathcal{B}(t, \theta, \phi, \sigma, E_p) = \mathcal{B}_{\text{time}} \times \mathcal{B}_{\text{space}} \times \mathcal{B}_E \quad (1.1)$$

In the following, data-based background PDFs are illustrated for the IceCube all-sky ten year point source dataset ('ps tracks version v003-p02') [4].

Background Time PDF

The IceCube detector is characterised by extremely high uptime of >99%, divided into runs separated by small downtime breaks. Even after processing to final-level event selections, samples typically consists of live-time at >90%, with the remaining time lost to partial detector operation, testing or temporary DOM failure. The arrival time of background events in Icecube is typically *assumed to be uniform during detector uptime*. This is again only approximately true, as evidenced by Figure 1.1. Six peaks

[2]: Aartsen et al. (2017), "The IceCube Neutrino Observatory: Instrumentation and Online Systems"

[3]: IceCube Collaboration et al. (2018), "Search for steady point-like sources in the astrophysical muon neutrino flux with 8 years of IceCube data"

[4]: Aartsen et al. (2020), "Time-Integrated Neutrino Source Searches with 10 Years of IceCube Data"

[5]: Heix et al. (2019), “Seasonal Variation of Atmospheric Neutrinos in IceCube”

corresponding to winters in the northern hemisphere are clearly visible, corresponding to $\pm \sim 5\%$ rate variations.

The atmospheric background rates depend on atmospheric densities which are ultimately temperature-dependent, leading to seasonal variations and clearly-visible annual cycles. This variation is itself an area of scientific interest, being exploited to measure climate variations with neutrinos [5]. These effects are partially mitigated in data-based models by the standard method of shuffling measured neutrino arrival times rather than drawing them from a PDF. In any case, the arrival time anisotropy is a small one.

Given this, we can approximate the background time PDF as uniform over periods of detector operation, with normalisation:

$$\mathcal{B}_{\text{time}} \approx \frac{1}{\text{livetime}} \quad (1.2)$$

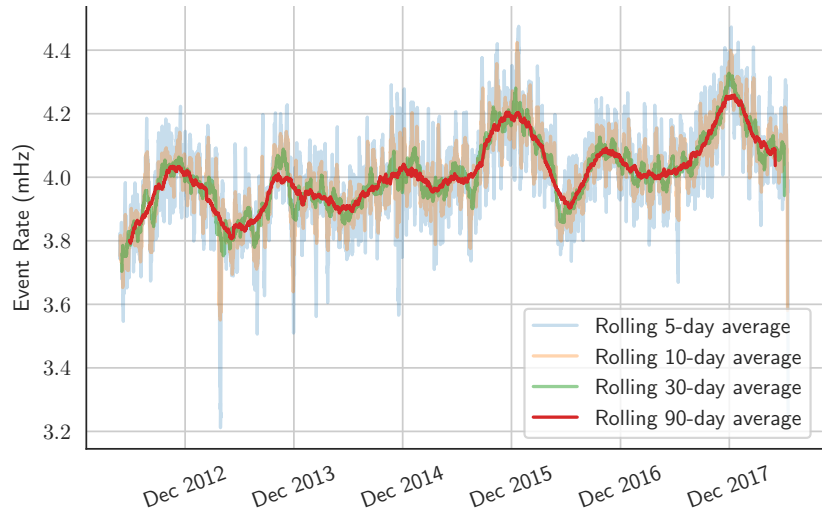


Figure 1.1: Rolling average of final-level event rate during detector uptime.

Background Spatial PDF

The spatial distribution of the background can be neatly factorised into two distinct components, namely a zenith and an azimuth component:

$$\mathcal{B}_{\text{space}}(\theta, \phi) = \mathcal{B}_\theta(\theta) \times \mathcal{B}_\phi(\phi, \theta) \quad (1.3)$$

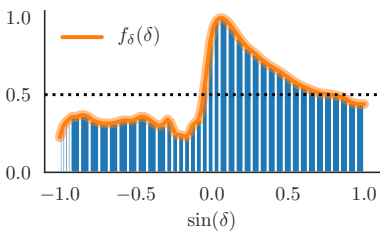


Figure 1.2: Event rate as a function of $\sin(\delta)$.

Owing to IceCube’s convenient location at the geographic south pole, the zenith-dependent detector response can be uniquely mapped into a declination-dependent one. With a data-driven background model, we can define a PDF $f_\delta(\delta)$ based on the declination-dependent event rate, as seen in Figure 1.2.

$$\mathcal{B}_\delta(\delta) = f_\delta(\delta) \quad (1.4)$$

The additional azimuthal component can be seen in Figure 1.3. The detector itself (see Chapter ??) has 6 string axes, and these are clearly visible with elevated event rates. These variations reach up to $\sim 40\%$

variations for the southern hemisphere. Additionally, the impact of *ice anisotropy* can be seen from an event rate deficit at and below the horizon [6], aligned with the axes of maximal charge deficit at $\sim 2\pi/3$ and $5\pi/3$.

However, string axes will all be traced out over the course of each day. Thus, for typical data periods of many years, these azimuthal variations will be averaged out. It is therefore typically assumed that *any variations due to azimuthal asymmetry are negligible*. An exception must be made for searches targeting clustering over short (sub-day) time periods, where this azimuthal asymmetry may have an impact. Beyond this, as long as the azimuth asymmetry can be neglected, we then find that the distribution in right ascension is uniform:

$$\mathcal{B}(\alpha) = \frac{1}{2\pi} \quad (1.5)$$

By substituting Equations 1.4 and 1.5, we can then replace Equation 1.3 with:

$$\mathcal{B}_{\text{space}}(\delta) = \frac{1}{2\pi} \times f(\delta) \quad (1.6)$$

Background Energy PDF

Having factorised the declination dependence of events in equation 1.4, we can then consider the expected energy proxy distribution for a given spatial position. The normalised energy proxy distribution as a function of $\sin(\delta)$ is given in Figure 1.4, with the median and central 90% ranges marked by dotted lines. It is clear that in the northern hemisphere, this distribution is essentially flat, reflecting the homogeneity of atmospheric neutrino backgrounds in this regime. However, the median energy proxy swiftly increases into the southern hemisphere, as more aggressive cuts are employed to remove the additional atmospheric muon background. The final turnover at the pole reflects the impact of the IceTop surface detector, which can be used to veto muon bundles from vertically-inclined showers.

In contrast to the strong declination dependence, Figure 1.5 shows that there is no azimuthal dependence for events in the northern hemisphere, and negligible variation in the southern hemisphere. We can thus construct simple two-dimensional background energy PDFs using the distribution shown in Figure 1.4:

$$\mathcal{B}_E(\delta, E_{\text{proxy}}) = f_E(E_{\text{proxy}}, \delta) \quad (1.7)$$

1.3 Signal Hypothesis

Signal hypotheses in IceCube are a composite of the background model with a small number of additional signal-like neutrinos (n_s). It is assumed that *the total number of neutrino events is essentially fixed by background*,

[6]: Chirkin et al. (2019), “Light diffusion in birefringent polycrystals and the IceCube ice anisotropy”

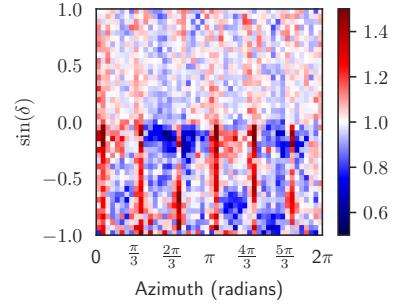


Figure 1.3: Declination-normalised event rate as a function of azimuth.

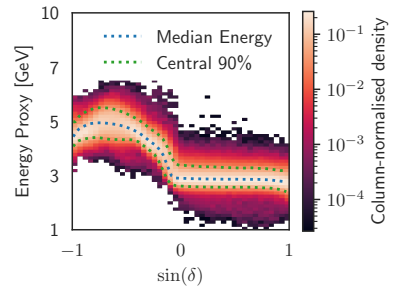


Figure 1.4: Background energy proxy distribution, normalised in bins of $\sin(\delta)$.

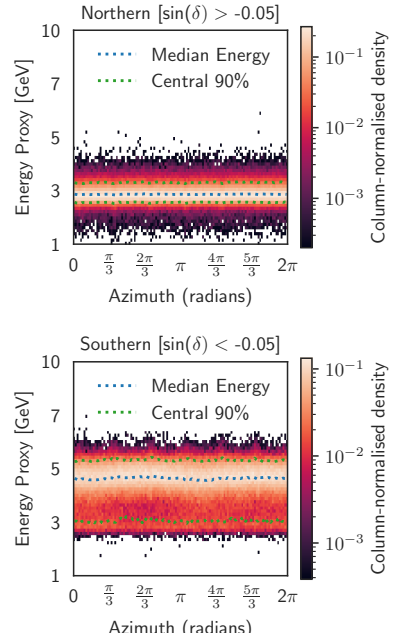


Figure 1.5: Background energy proxy distribution, normalised in bins of azimuth.

so that $N = n_s + n_b$. In this case, we define our signal hypothesis as the normalised sum of a background PDF \mathcal{B} and signal PDF \mathcal{S} :

$$\mathcal{H} = \frac{n_s}{N} \mathcal{S} + \frac{N - n_s}{N} \mathcal{B} \quad (1.8)$$

Much like the background, the signal PDF is a product of energy, temporal and spatial PDFs:

$$\mathcal{S} = \mathcal{S}_{\text{time}} \times \mathcal{S}_{\text{space}} \times \mathcal{S}_{\text{E}} \quad (1.9)$$

In IceCube, it is common to test hypotheses in which the number of signal neutrinos, n_s , is a free parameter. It is also common to assume that the intrinsic signal energy PDF is an unbroken power law with some spectral index, $E^{-\gamma}$, where the spectral index γ is an additional free parameter.

Signal Time PDF

In almost all IceCube analyses, the signal time PDF is assumed to be a uniform distribution over a fixed period of livetime. This could be for the entire duration of a dataset, corresponding to a steady neutrino source. This special case is typically referred to as a *time-integrated analysis*, because it cancels out exactly the assumed background time PDF, yielding a likelihood that does not depend on time. This thesis is concerned with *transient* sources, which are only active over fixed periods of time. Transient source hypotheses require a *time-dependent analysis*, in which the signal is not assumed to be uniform over the full data-taking duration.

The uptime of the detector can be characterised by a boolean detector response function, $f_{\text{uptime}}(t)$, that is either on (1) or off (0). The signal time PDF is then a product of the underlying source PDF and this detector response PDF. For this thesis, the only relevant transient time PDF was a simple *box model*. This is a uniform signal normalised over the livetime, Δ_T , between start time T_0 and end time T_1 :

$$\Delta_T = \int_{T_0}^{T_1} f_{\text{uptime}}(t) dt \quad (1.10)$$

$$\mathcal{S}_{\text{time}}(t) = \begin{cases} f_{\text{uptime}}(t) \times \frac{1}{\Delta_T} & T_0 < t < T_1 \\ 0 & \text{otherwise} \end{cases} \quad (1.11)$$

Signal Spatial PDF

The standard spatial signal PDF is typically stated to be *the assumption of a circular Gaussian PSF centered on the position of a source*. For an event at \vec{x} with a localisation uncertainty σ and a source at position \vec{d} , we then have:

$$r^2 = (\vec{x} - \vec{d})^2 \quad (1.12)$$

$$\mathcal{S}_{\text{space}}(\vec{x}) = \frac{1}{2\pi\sigma^2} e^{-r^2/2\sigma^2} \quad (1.13)$$

In reality, even under the limit of a perfect muon track reconstruction, the unmeasurable energy-dependent kinematic angle between the incoming neutrino and outgoing muon will limit the resolution of any search. The signal PSF thus depends on the signal hypothesis, where higher-energy neutrinos are better reconstructed even for fixed σ .

Ultimately, the performance of directional reconstructions is verified on MC events, and energy-dependent biases in uncertainty estimates are corrected in a process known as pull corrections (see Chapter ??). So, more precisely, the signal spatial PDF is *assumed to follow the distribution found in baseline MC simulations weighted with an unbroken E^{-2} power law*, and further *it is assumed that this distribution can be approximated by a circular Gaussian PSF with a single per-event energy-corrected uncertainty parameter*. The first assumption clearly requires that the impact of systematic uncertainties on MC simulation is negligible. The validity of these assumptions is discussed further in Chapter N, but it should be noted that neither approximation is completely valid.

A Gaussian term for the spatial PDF also indirectly *assumes that the Signal PDF does not depend on azimuth*. It is clear in the left panels of Figure 1.6 that azimuthal asymmetry is increasingly visible for soft spectra in the northern hemisphere, and approximately resembles the pattern seen in Figure 1.3. However, for both the southern sky and a hard E^{-1} spectrum, there is no such asymmetry. As can be clearly seen in Figure 1.7, these corresponds to regimes where the signal is dominated by high-energy events. In general, *the effective area at lower energies is azimuth-dependent, while at higher energies it is approximately uniform*. This is because, at lower energies, only tracks which pass close to the DOMs will be detected. In any case, as can be seen in the right-hand panels of Figure 1.6, azimuth has very little discriminating power for any spectral index, and can thus be safely neglected for analysis.

Signal Energy Proxy PDF

The energy PDF is most commonly *assumed to be an unbroken power of index γ extending over the entire energy range of sensitivity for the IceCube detector*, namely from 100 GeV to 10 PeV. This energy spectrum is then convolved with the detector response function through use of weighted MC simulation, yielding an expected distribution of energy proxy values:

$$\mathcal{S}_E(\delta, E_p, \gamma) = f_E(\delta, E_p, \gamma) \quad (1.14)$$

An illustration of the expected signal distribution, derived from MC for a range of spectral indices, is illustrated in the left panels of Figure 1.7. It is clear that hard spectra result in events with energies substantially above those expected in background, but for softer spectra the distribution narrows and is much more similar to that in Figure 1.4. Much of the discriminating power in IceCube comes from the identification

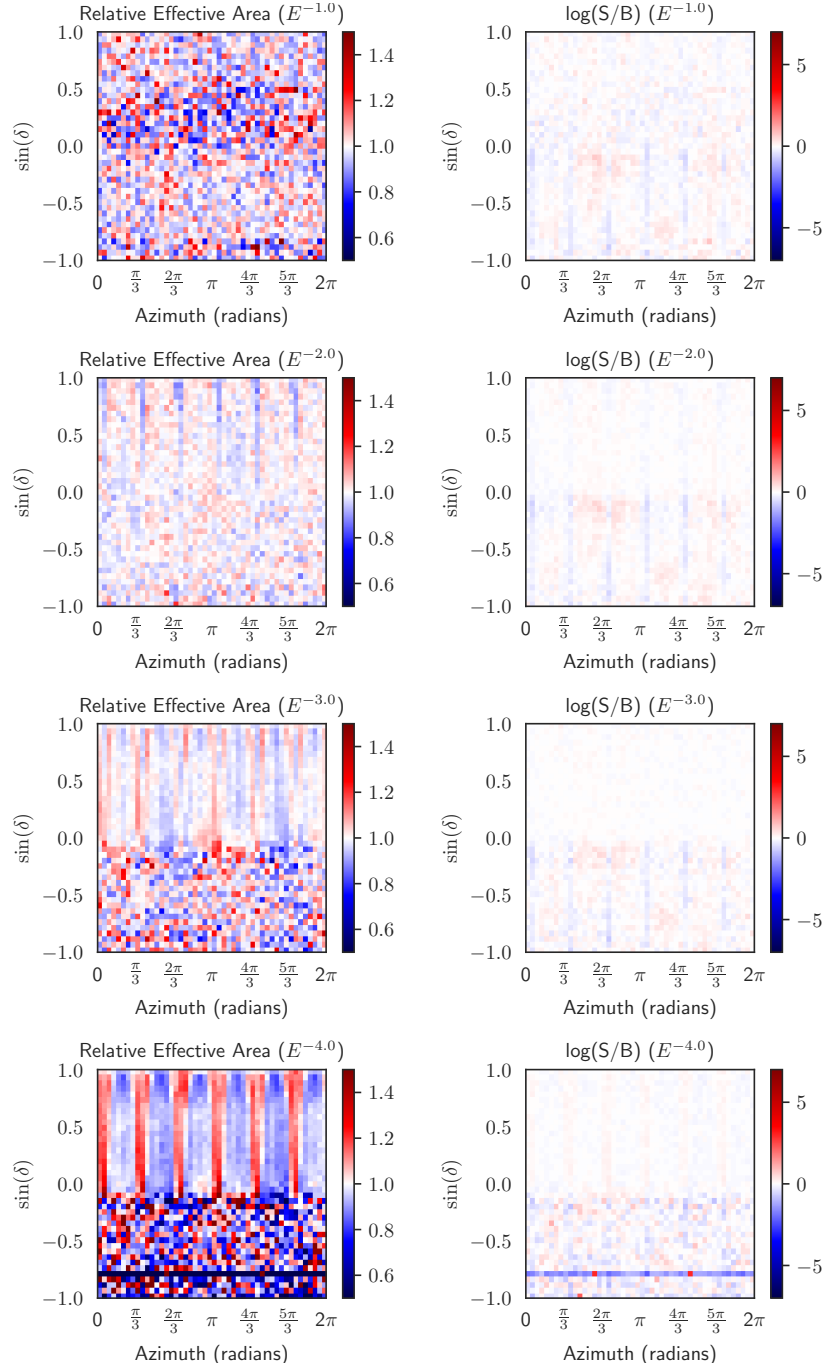


Figure 1.6: Left: Declination-normalised MC rate as a function of azimuth. Right: Ratio of declination-normalised Signal and Background PDFs.

of these high-energy neutrinos, which are unlikely to arise from atmospheric backgrounds but should arise from hard $\sim E^{-2}$ spectra expected for most astrophysical neutrino sources.

Similar to the spatial PDF, the signal energy proxy PDF *ultimately assumes that the baseline MC accurately describes the expected energy proxy distribution*. This again implicitly assumes that systematic uncertainties have a negligible impact on energy proxy distributions.

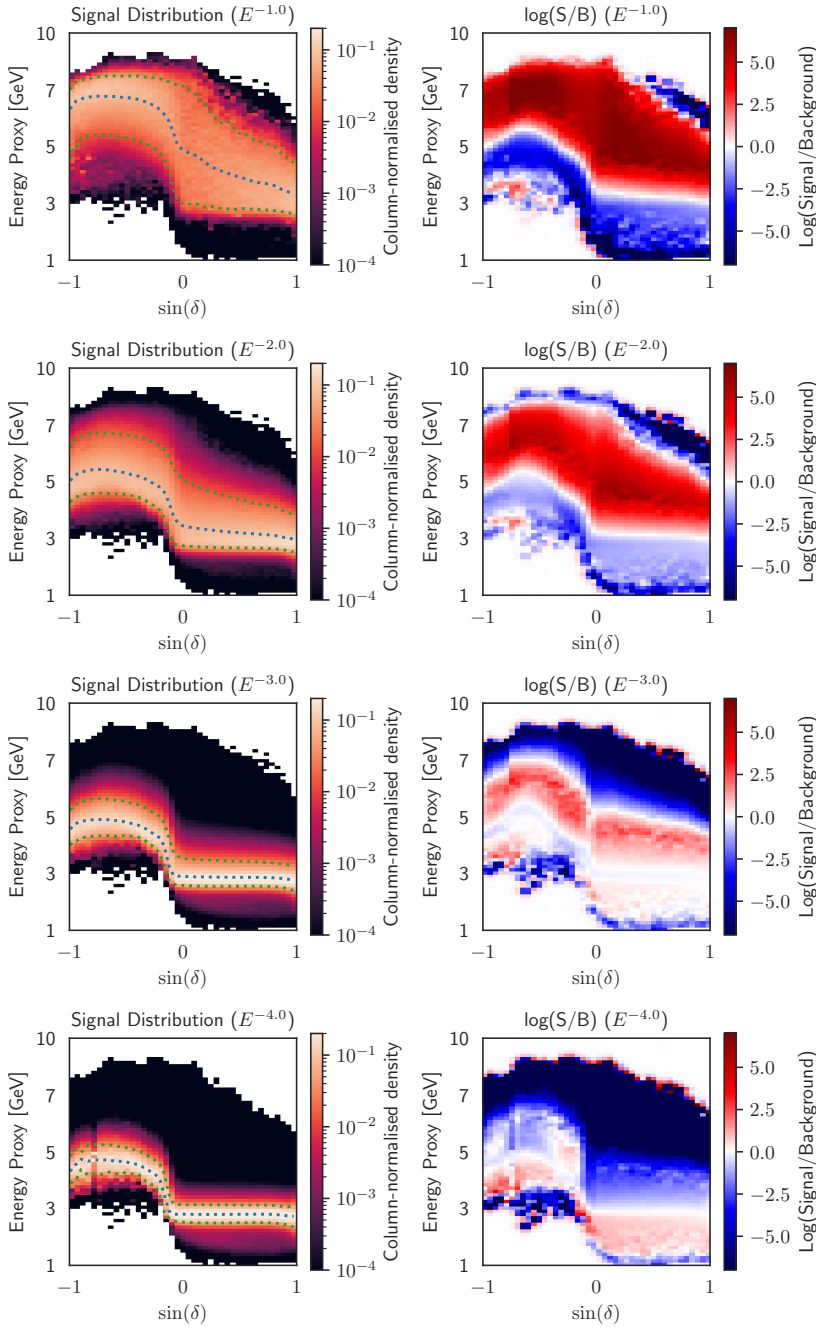


Figure 1.7: Left: Energy proxy distribution as a function of $\sin(\delta)$, for various signal hypotheses. Right: Ratio of declination-normalised Signal and Background PDFs.

1.4 Likelihoods and Wilk's Theorem

One method of quantifying agreement between a hypothesis and data is to calculate the *likelihood*, \mathcal{L} , of observing our data given that hypothesis. Using the PDFs describing how we would expect observables to be distributed for each hypothesis, we can calculate the conditional probability, $\mathcal{L}(x|\mathcal{H})$, of observing our data x given that hypothesis. The likelihood values can be used to construct a test statistic:

$$TS(\mathcal{H}_i) = 2 \log \left(\frac{\mathcal{L}(x|\mathcal{H}_i)}{\mathcal{L}(x|\mathcal{H}_0)} \right) \quad (1.15)$$

The primary motivation for using this test statistic definition comes from

[7]: Neyman et al. (1933), “On the Problem of the Most Efficient Tests of Statistical Hypotheses”

[8]: Braun et al. (2008), “Methods for point source analysis in high energy neutrino telescopes”

the *Neyman-Pearson Lemma* [7], which states that the likelihood ratio test is the most powerful possible statistical test.

While this TS definition could be used for a likelihood that is evaluated for discrete regions of parameter space (a *Binned likelihood analysis*), it has long been customary in IceCube to instead evaluate the likelihood in a continuous event-wise fashion (an *Unbinned likelihood analysis*) [8]. A likelihood is constructed, and evaluated for each j th individual event, with the overall likelihood given by the product of these N independent events:

$$\mathcal{L} = \prod_i^N \mathcal{L}_i \quad (1.16)$$

Ultimately this yields the standard *Point Source Likelihood*:

$$\mathcal{L}(n_s, \gamma) = \prod_i^N \left(\frac{n_s}{N} \mathcal{S}(\theta_i, \gamma) + \frac{N - n_s}{N} \mathcal{B}(\theta_i) \right) \quad (1.17)$$

We are thus testing a continuum of hypotheses parameterised by n_s and γ , where both \mathcal{S} and \mathcal{B} depend on the event-specific observables θ_j . We typically construct the negative log likelihood ($-\log \mathcal{L}$), and then derive best-fit parameters \hat{n}_s and $\hat{\gamma}$ by a process of maximum likelihood estimation. We take the combination of parameters which maximises the likelihood, and use this as our final TS value.

1.5 Pseudo-trials, P-values and trial corrections

Given a particular TS value, we must then calculate a p-value to quantify whether or not the null hypothesis can be rejected. The most simplistic method is to perform simulated *pseudo-experiments* based on the null hypothesis, to quantify how often a given outcome occurs. This method critically relies on the assumption that *pseudo-experiments can be accurately simulated, and thus represent the expected distribution*.

Much like for Section 1.2, the null distribution can be simulated using either a data-based or MC-based model. In general, for any point source analysis, data-based methods perform well because the datasets are indeed background-dominated. Furthermore, the data can be easily randomised through use of *data-scrambling*, in which the detector symmetry is exploited by randomly assigning new values of right ascension to events. Furthermore, relying on the assumption that *the dataset is background-dominated at all relevant timescales*, the temporal variations of the background shown in Figure 1.1 can easily be accounted for by randomly reassigning the arrival time of events to other events. These methods work principally because a point source analysis is concerned with only a tiny fraction of the data, in a narrow right ascension/declination range, and thus the broader population distribution is almost completely independent of any signal hypothesis. Alternatively using MC-based models ensures there is absolutely no contamination of the background distribution with signal, but comes at the cost of introducing a dependence on the data-MC agreement for any subsequent conclusions.

An alternative method of calculating a p-value is to exploit Wilk's Theorem [9]. Wilk's Theorem states that the log likelihood ratio for an ensemble of datasets will be distributed according to a χ^2 distribution, with degrees of freedom equal to the number of independent parameters. Thus, for a hypothesis depending on a known number of independent parameters, we can analytically convert any TS value to a *p-value*. There are, however, caveats to Wilk's Theorem. The full formulation only applies in the limit of large samples, and in the absence of bounds on fit parameters. In IceCube this condition is usually satisfied, but there are exceptions particularly for searches on short-timescales relevant for GRB or FRB searches, where the data transitions from a background-dominated regime to a background-free one.

For most cases, including all analysis for this thesis, a hybrid approach is used. A large number of pseudotrials are generated, providing an ensemble of TS values. A χ^2 distribution is then fit to this dataset, with the degrees of freedom and normalisation being free parameters. This fitted distribution can then be used to extrapolate from the experimental distribution (typically several hundred thousand) to even smaller p-values, such as for the 5σ TS value which would otherwise require several million trials.

An example distribution, for a source at the horizon, is illustrated in Figure 1.8. It is well-fit by the χ^2 distribution, with ~ 1.4 degrees of freedom. Though this may appear to be unphysical, it illustrates the fact that the likelihood outlined in Equation 1.17 does not have two independent fit parameters. Rather, given that PS analyses search primarily for an excess of high-energy neutrinos, n_s and γ are in fact degenerate to a large degree. From the perspective of a likelihood analysis, a single high-energy neutrino on top of an abundant low-energy background does not appear very different to a single high-energy neutrino with a handful of lower-energy neutrinos against an abundant low-energy background. As can be seen in Figure 1.9, for a Point Source Likelihood without energy terms, the TS distribution is well fit by a χ^2 distribution with exactly 1 degree of freedom, as expected for a likelihood that depends only on n_s .

For a single hypothesis, the procedure would then be complete. However, it is common that multiple hypotheses are tested at once, for example in this thesis with multiple catalogues (see Chapter 2). Given that each independent test has a probability to randomly produce an overfluctuation, smaller p-values become increasingly likely as more tests are added. To counteract the multiple hypothesis problem, known as the *look-elsewhere effect*, a correction must be introduced, known as a *trial factor*. The trial factor quantifies the number of independent tests that have been performed, and thus quantifies how likely it is to find a small p-value. If the smallest pre-trial p-value is $p_{\text{pre-trial}}$, then for N independent trials we find:

$$p_{\text{post-trial}} = 1 - \left(1 - p_{\text{pre-trial}}\right)^N \quad (1.18)$$

Defining what constitutes an independent trial can be difficult. It is a common misconception that the trial factor is particularly important for cases when two hypotheses are similar. In the limit that two hypotheses are so similar as to be essentially identical, there would be no need for

[9]: Wilks (1938), "The Large-Sample Distribution of the Likelihood Ratio for Testing Composite Hypotheses"

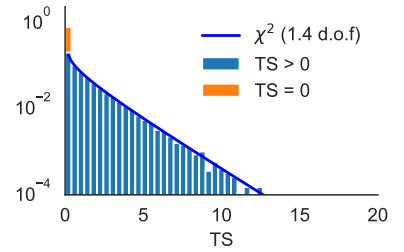


Figure 1.8: Background TS distribution for the standard Point Source Likelihood (Equation 1.17).

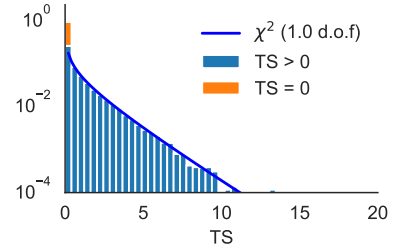


Figure 1.9: Background TS distribution for a Point Source Likelihood without an energy term.

a trial correction at all, since the test statistic for each would be identical. The trial factor should correct the degree to which hypotheses are capable of giving multiple independent TS values. Distinct catalogues which do not share sources are completely independent trials, and thus N is simply the number of source lists tested. For correlated tests, such as overlapping catalogues or identical catalogues with different intrinsic source weighting, the trial factor will always be smaller than the number of tests but there is no analytic solution to the exact factor. Instead, it can in principle be derived experimentally, by performing all tests on each pseudo-trial, and considering the distribution of smallest p-values. In this thesis, the conservative approach is employed instead, by counting tests and assuming they are independent.

1.6 Sensitivities, Discovery Potentials and Upper Limits

When developing and performing statistical analysis, we often wish to quantify how powerful a particular test is. As an extension of the background pseudo-experiments outlined in Section 1.5, we can also perform pseudo-experiments with our signal hypothesis. This is done through the process of *signal injection*, whereby a pseudo-dataset is constructed using a combination of the background model and a signal model. The resulting TS distribution, and all conclusions derived from it, again introduce an assumption that *the baseline MC can be used to represent signal*.

With a signal TS distribution, we can characterise the power of our test by assessing the degree to which the signal TS distribution differs from the background one. For a given p-value threshold, as defined by the background model, we can calculate how frequently a given signal hypothesis would lead to a rejection of the null hypothesis. This yields the Type II error rate for any test.

The principle can be extended to cover multiple hypotheses. In the case of neutrino astronomy, a signal hypothesis can be defined for any number of signal neutrinos, n_{inj} , that are injected. Since the detection of neutrinos is a random process, the number of signal neutrinos can be simulated with a poisson process of mean n_{exp} . We can thus parameterise a continuous set of signal hypotheses as a function of n_{exp} , under the assumption of a given spectral model.

An example signal TS distribution can be seen in Figure 1.10, which covers the same time-integrated horizon source shown in Figure 1.8 with the addition of ≈ 3 injected signal neutrinos. The signal TS distribution is notably shifted to higher TS values, with only 6% of trials yielding a TS=0. The same trend is seen for Figure 1.11, with the same number of injected signal neutrinos using a spatial-only likelihood.

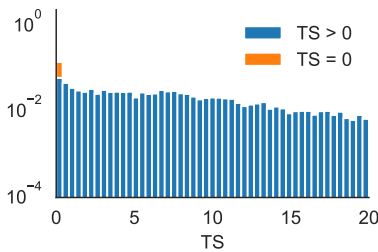


Figure 1.10: Signal TS distribution for the standard Point Source Likelihood (Equation 1.17), with ≈ 3 injected neutrinos.

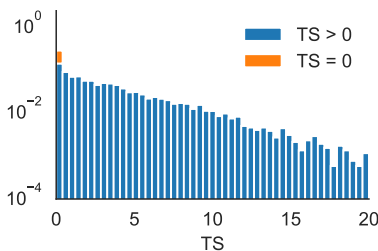


Figure 1.11: Signal TS distribution for the Point Source Likelihood without an energy term, with ≈ 3 injected neutrinos.

It is often useful to quantify the rate of both Type I and Type II errors associated with different regions of parameter space, especially those which rely on n_{exp} . One example is the *sensitivity* of a test, defined as the value of n_{exp} for which 90% of the signal trials will yield a TS value greater than the background median. Here the Type I error rate is 50%, and the Type II error rate is 10%.

Another common metric is the *median 5 σ discovery potential*. This is the value of n_{exp} for which 50% of the signal trials will yield a p-value exceeding the 5 σ threshold. In this case, the Type I error rate is $\approx 3 \times 10^{-7}$, while the Type II error rate is 50%. The 5 σ discovery potential illustrates the region of signal parameter space for which a discovery could be expected.

An example of the sensitivity is shown in Figure 1.12, using the background median threshold (TS=0.0) from the distribution in Figure 1.8. For comparison, the spatial-only sensitivity is shown in Figure 1.13, relative to the corresponding background median distribution (TS=0.0) in Figure 1.9. While the standard Point Source Likelihood (Equation 1.17) has a sensitivity of ≈ 3 signal neutrinos, the spatial-only likelihood has a sensitivity of ≈ 4 signal neutrinos. The latter method thus requires $\approx 33\%$ more signal to produce a ‘likely detection’, illustrating the enhanced power of the energy-dependent Point Source Likelihood as a statistical test. The discrepancy is even more extreme for discovery potential, with the standard method requiring ≈ 10 neutrinos (Figure 1.14) whereas the spatial-only method requires ≈ 18 neutrinos (using the extrapolation in Figure 1.15).

These metrics allow us quantify the performance of a test without requiring knowledge of the actual outcome of the test on real data. In this way, an analysis can be designed that is *blind*, and thus free from human bias. We optimise our analysis in terms of achieving the best possible sensitivity or discovery potential, and only then do we perform the test on real data. Applying this principle to the two cases outlined above, it clear that we should use the Point Source Likelihood with an energy term, and this conclusion has been reached without knowledge of the ultimate outcome of either test on the real dataset.

Once the analysis has been *unblinded*, we can also recycle these pseudo-experiments to set an upper limit. Following exactly the same procedure as for sensitivity, we can derive an upper limit at some confidence level, typically 90%, using the observed TS value and our pseudo-experiments with added signal. Our upper limit is defined as the signal expectation for which 90% of the pseudo-experiments would yield a TS greater than or equal to the value observed. By construction, for a median experimental result of the background hypothesis, the upper limit derived at 90% confidence level is exactly equal to the sensitivity. Conventionally, in IceCube, for results which yield an underfluctuation relative to background expectations (a TS value less than the median), the sensitivity is quoted as an upper limit.

Both sensitivity and discovery potential can be used to characterise and compare the relative power of statistics tests, in terms of signal events. However, through use of the effective area, $A_{\text{eff}}(\delta)$, we can convert these values of n_{exp} into corresponding values of muon neutrino flux normalisation.

Under the assumption that *the effective area, as derived with baseline MC, is an accurate description of the detector*, we then find for a flux of normalisation ϕ_0 :

$$n_{\text{exp}}(\gamma) = \phi_0 \int \mathcal{S}_{\text{time}}(t) dt \int A_{\text{eff}}(\delta, E_\nu) \times E_\nu^{-\gamma} dE_\nu \quad (1.19)$$

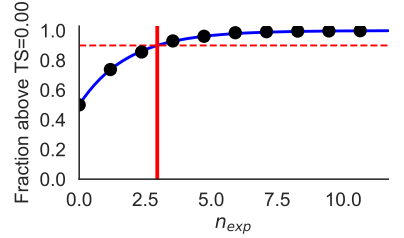


Figure 1.12: Sensitivity for the standard Point Source Likelihood (Equation 1.17), using the background TS distribution from Figure 1.8.

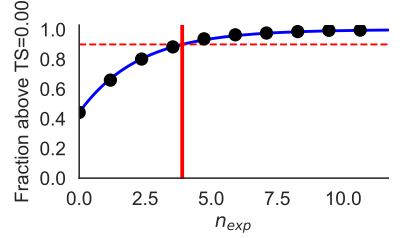


Figure 1.13: Sensitivity for the Point Source Likelihood without an energy term, using the background TS distribution from Figure 1.9.

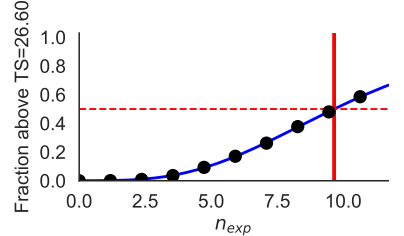


Figure 1.14: 5 σ Discovery Potential for the standard Point Source Likelihood (Equation 1.17), using background TS distribution from Figure 1.8.

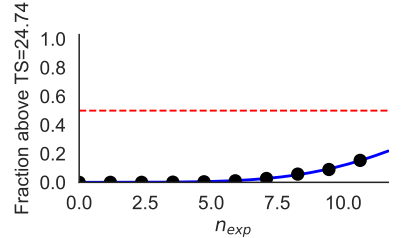


Figure 1.15: 5 σ Discovery Potential for the Point Source Likelihood without an energy term, using background TS distribution from Figure 1.9.

The effective area as a function of declination, $A_{\text{eff}}(\delta)$, is shown in Figure 1.16. The effective area is highest at the horizon (green lines), where it increases with neutrino energy. However, for more northern declination (yellow to red lines), the increasing impact of earth absorption suppresses neutrino detection at energies greater than 100 TeV. For the southern hemisphere, increasingly aggressive cuts to reject atmospheric muons mean that the effective area is also lower overall (blue lines), though as with the horizon there is no earth absorption of neutrinos.

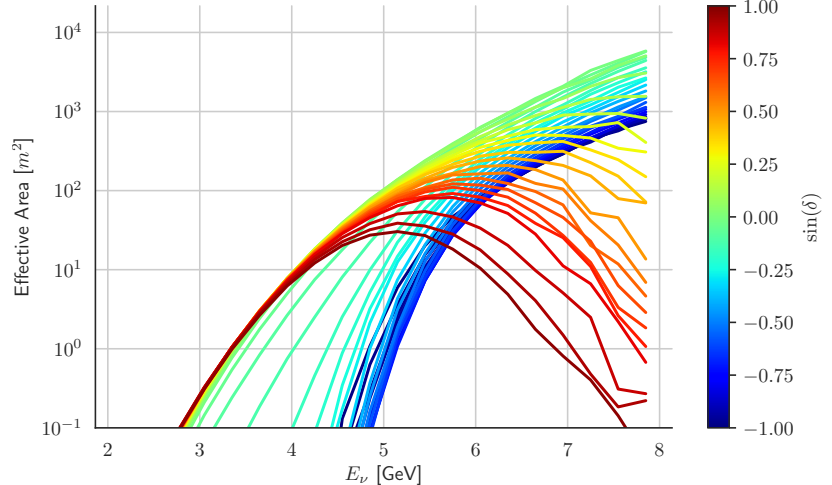


Figure 1.16: Effective area as a function of neutrino energy and declination.

With Equation 1.19, we can then characterise the properties of astrophysical neutrino sources for which we could expect a discovery, and conversely we can constrain these properties for a null result. This is illustrated in Figure 1.17, illustrating the sensitivity and 5σ discovery potential for a point source at various declinations. The values are derived using the full Point Source Likelihood introduced in Equation 1.17, including an energy term. As expected from Figure 1.16, the detector is most sensitive at the horizon but gradually deteriorates at more northern declinations due to increasing Earth absorption. Below the horizon, the sensitivity rapidly deteriorates due to the higher muon background.

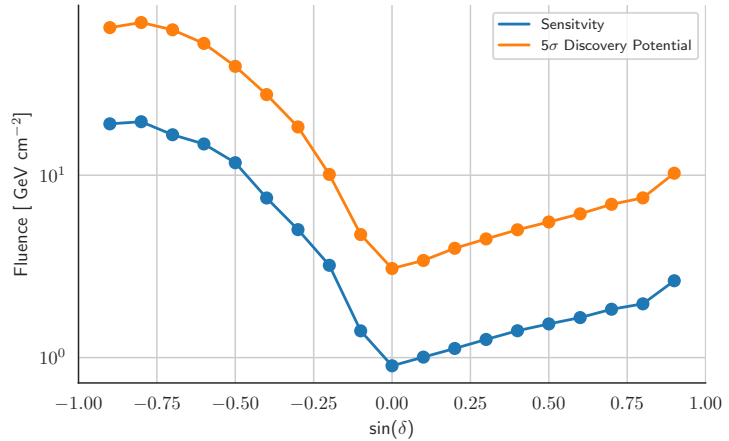


Figure 1.17: Sensitivity and Discovery potential as a function of declination for an E^{-2} spectrum.

1.7 Stacking Multiple Sources

The simple source hypothesis outlined in Equation 1.8 describes a single source, but can easily be expanded to include an ensemble of sources, known as a *Stacking Analysis*. For a multi-source hypothesis, the relative contribution of each source must be accounted for.

In most cases, it is *assumed that all sources share the same intrinsic neutrino spectrum*. A further assumption must be made on the fraction of catalogue flux, f_k , that each kth source will contribute. One common assumption is *equal weights*, so that each of M sources contributes equally:

$$f_k = \frac{1}{M} \quad (1.20)$$

Alternatively, another common assumption is *standard candles*, where the intrinsic luminosity of each source is equal. For each kth source at luminosity distance $D_{L,k}$

$$f_k = \frac{1/D_{L,k}^2}{\sum_{k=1}^M (1/D_{L,k}^2)} \quad (1.21)$$

In any case, we can then calculate the expected number of signal neutrinos, n_k , for each source:

$$\phi_k = \phi_0 \times f_k \quad (1.22)$$

$$n_k(\gamma) = \phi_0 f_k \int \mathcal{S}_{\text{time}, k}(t) dt \int A_{eff}(\delta_k, E_\nu) \times E_\nu^{-\gamma} dE_\nu \quad (1.23)$$

Using Equation 1.23, we can then define the fractional source weight, w_k , of each kth source:

$$w_k(\gamma) = \frac{n_k(\gamma)}{\sum_{k=1}^M n_k(\gamma)} = \frac{f_k \int \mathcal{S}_{\text{time}, k}(t) dt \int A_{eff}(\delta_k, E_\nu) \times E_\nu^{-\gamma} dE_\nu}{\sum_{k=1}^M (f_k \int \mathcal{S}_{\text{time}, k}(t) dt \int A_{eff}(\delta_k, E_\nu) \times E_\nu^{-\gamma} dE_\nu)} \quad (1.24)$$

Unlike for Equation 1.23, w_k does not ultimately depend on the flux normalisation ϕ_0 . For fixed spectral index, the relative contribution of different sources is independent of the number of neutrinos. Using these source weights, we can then define our normalised Signal model:

$$\mathcal{S}(\gamma) = \sum_{k=1}^M (w_k(\gamma) \times \mathcal{S}_k(\gamma)) \quad (1.25)$$

Substituting this into Equation 1.17, we arrive at our stacked PS likelihood. Conveniently, $\mathcal{S}_E(\gamma)$ does not vary by source, so can be factorised out of the sum. For steady neutrino sources, $\mathcal{S}_{\text{time}}$ can also be factorised out, leaving only a sum over $\mathcal{S}_{\text{space}, k}$.

1.8 Combining seasons

We can generalise the procedure even further, to account for multiple IceCube seasons. As outlined in Chapter ??, the IceCube detector was constructed in phases, with multiple partial detector configurations each operating for roughly one year. It is conventional, as for *ps tracks v003*, to include data from IC40, IC59, IC79, and IC86, where ICn refers to the number of detector strings, n, in operation. The first year of IC86, (IC86-2011), corresponded to a different set of detector triggers, and is treated distinctly from IC86 for seasons 2012 and upward. Thus there are ultimately five distinct sets of detector operation in the ten-year point source dataset, each with a unique event selection.

These J seasons can be combined by treating them as independent datasets, and combining the likelihood for each ith neutrino in each jth season:

$$\mathcal{L} = \prod_j^J \prod_i^N \mathcal{L}_{i,j} \quad (1.26)$$

The procedure outlined in Sections 1.2 and 1.3 is followed for each dataset, yielding season-specific PDFs. The signal hypothesis can be divided in much the same way as for stacking, with a separate time PDF covering the uptime for each season ($t_{0,j} - t_{1,j}$). Then, for each kth source and jth season:

$$n_{j,k}(\gamma) = \phi_0 \int_{t_{0,j}}^{t_{1,j}} \mathcal{S}_{\text{time, j, k}}(t) dt \int A_{eff,j}(\delta_k, E_\nu) \times E_\nu^{-\gamma} dE_\nu \quad (1.27)$$

$$\mathcal{S}_j(\gamma) = \sum_{k=1}^M (w_{k,j}(\gamma) \times \mathcal{S}_{j,k}(\gamma)) \quad (1.28)$$

$$n_j(\gamma) = n_s \sum_{k=1}^M w_{k,j}(\gamma) \quad (1.29)$$

$$\mathcal{L}(n_s, \gamma) = \prod_j^J \prod_i^N \left(\frac{n_j}{N} \mathcal{S}_j(\theta_i, \gamma) + \frac{N - n_j}{N} \mathcal{B}_j(\theta_i) \right) \quad (1.30)$$

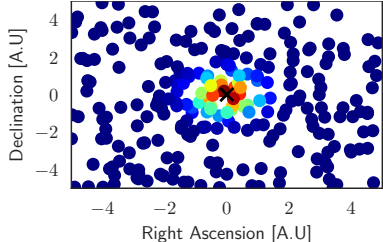


Figure 1.18: Visualisation of a spatial PDF.

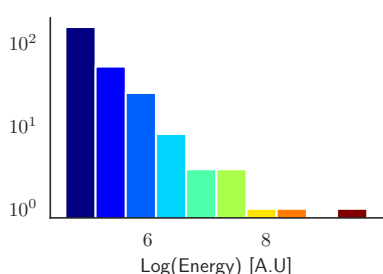


Figure 1.19: Visualisation of an energy proxy PDF.

1.9 Cluster-search algorithm

One possible modification to the likelihood outlined above is to search for neutrino emission that is clustered in time, within a larger search window. The procedure is implemented in `flarestack`, and is used in this thesis for analysis of some sources.

Multiple box time PDFs are tested for a given source, and the one with the highest TS value is selected. Flares have both a start point, T_0 , and end point, T_1 , yielding two additional fit parameters. However, the likelihood landscape has discontinuities from when single neutrinos passing in/out boundary of the time PDF. Therefore, to avoid issues with minimisation

by gradient descent, in *flarestack* the optimal flare is selected through a brute-force minimisation procedure. Though T_0 and T_1 are in principle continuous variables, the most significant possible cluster will always be one that begins and ends with the detection of a neutrino.

However, for N neutrinos in a dataset, there are $N \times (N - 1)/2$ possible pairs to test. To further speed computation, a simplifying assumption is made that *the most significant cluster will begin and end with signal-like neutrinos*. The \mathcal{S}/\mathcal{B} ratio is calculated for all neutrinos, and only those with $\mathcal{S} > \mathcal{B}$ are considered sufficiently signal-like to test. This procedure is illustrated in Figure 1.20.

However, there is an inherent bias in such a cluster search, because there are many possible small clusters in a search window but very few possible large ones. Background fluctuations are preferentially found as small clusters. To counter this effect, a marginalisation term must be introduced to balance this bias, yielding a *flare likelihood*. For a search window between t_0 and t_1 , with a flare from T_0 to T_1 , we find:

$$\Delta_{T, \text{flare}} = \int_{T_0}^{T_1} f_{\text{uptime}}(t) dt \quad (1.31)$$

$$\Delta_{T, \text{search}} = \int_{t_0}^{t_1} f_{\text{uptime}}(t) dt \quad (1.32)$$

$$\mathcal{L}(n_s, \gamma, T_0, T_1) = \prod_i^N \left(\frac{n_s}{N} \mathcal{S}(\theta_i, \gamma, T_0, T_1) + \frac{N - n_s}{N} \mathcal{B}(\theta_i) \right) \times \frac{\Delta_{T, \text{flare}}}{\Delta_{T, \text{search}}} \quad (1.33)$$

An example of this cluster search, as used for the source AT2018cow (see Chapter 2), demonstrates the impact on discovery potential. Given the additional degrees of freedom, there is more scope for background fluctuations, so the threshold for discovery is higher in the case that neutrino emission extends over the full search window. However, for shorter neutrino emission periods, the discovery potential is much reduced.

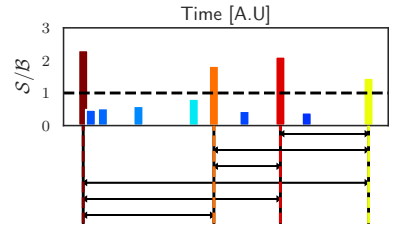


Figure 1.20: Visualisation of the cluster search algorithm.

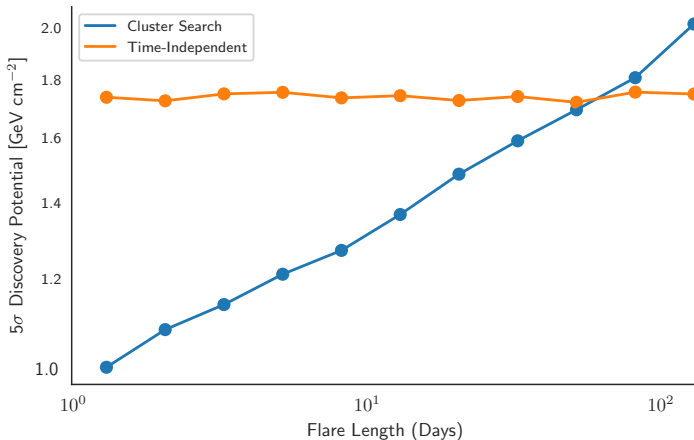


Figure 1.21: Estimated 5σ Discovery Potential for AT2018cow as a function of flare length, given in units of total fluence for an E^{-2} spectrum over the 130 day search window.

1.10 Fitting the relative source weights

The direct implementation of a well-defined \mathcal{S} for a stacking analysis is the most powerful possible test, *under the assumption that the relative distribution of the signal is known*. This condition can be satisfied when a specific model is tested that accurately predicts the relative number of signal events produced by each source in an ensemble. A prediction using multi-wavelength emission as a proxy, or expectations for a population of neutrino standard candles, are common assumptions. However, in an agnostic search for neutrino emission from a source ensemble, the uncertainty of our knowledge should be ideally implemented through priors on our expectations of neutrino emission from each source. The standard *Point Source Likelihood* can be thought of as one extreme with maximum knowledge yielding δ -function priors for the neutrino emission from each source. The other extreme is one of maximum ignorance, in which flat priors $n_{s,k}$ for each k th source is allowed to vary completely independently. In that case, we can replace the point-source likelihood (Equation 1.17) with the *multi-source likelihood*:

$$\mathcal{L}(\vec{n}_s, \gamma) = \prod_j^N \left(\sum_k \left[\frac{n_{s,k}}{N} \mathcal{S}_k(\theta_j, \gamma) \right] + \frac{N - \sum_k [n_{s,k}]}{N} \mathcal{B}(\theta_j) \right) \quad (1.34)$$

This approach is commonly referred to as *fitting the weights* of each source, in contrast to the standard method of *fixed source weights*. Additional flexibility comes at the expense of more independent fit parameters, and thus a higher TS threshold to achieve fixed significance. In the limit of many sources, each with sub-unity neutrino expectations, the number of degrees of freedom would exceed the number of expected signal events. It is most useful for analysing a small number of sources, in which the relative neutrino distribution is not known, but for which multiple neutrinos would be expected. This likelihood is used for some results in this thesis (see Chapter 2).

1.11 Flarestack in practice

The evaluation of this likelihood is time-consuming, and the implementation of this process in *flarestack* makes several standard simplifications to speed calculations [10].

[10]: Stasik (2017), “Search for High Energetic Neutrinos from Core Collapse Supernovae using the IceCube Neutrino Telescope”

The first is the recognition that the parameters which maximise the likelihood will also maximise the likelihood ratio, and thus the test statistic. Rather than evaluating two independent likelihoods, we can instead directly evaluate the test statistic:

$$TS = 2 \log \left(\frac{\mathcal{L}(\hat{n}_s, \hat{\gamma})}{\mathcal{L}(n_s = 0)} \right) \quad (1.35)$$

$$TS = 2 \log \frac{\prod_j^N \left(\frac{n_s}{N} \mathcal{S}(\theta_j, \gamma) + \frac{N-n_s}{N} \mathcal{B}(\theta_j) \right)}{\prod_j^N \mathcal{B}(\theta_j)} \quad (1.36)$$

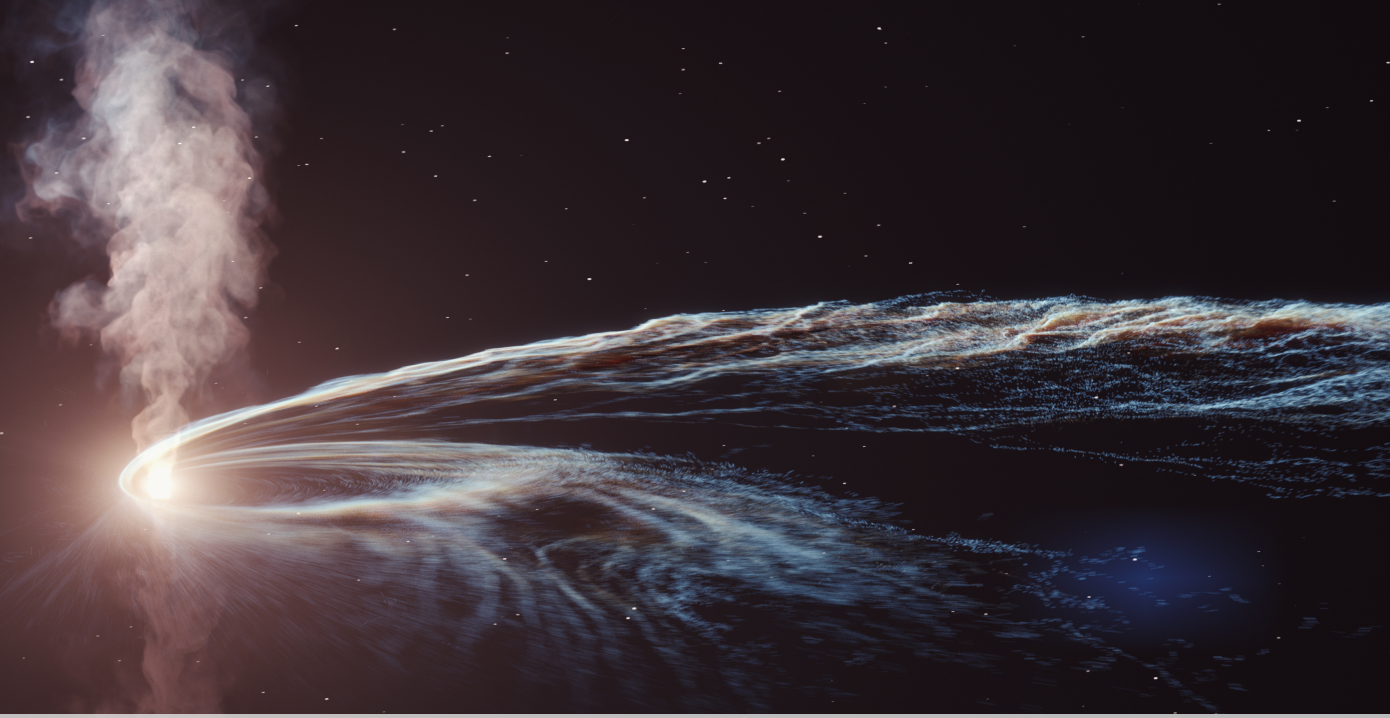
By dividing this through, we find:

$$TS = 2 \log \left(\prod_j^N \left(\frac{n_s}{N} \left[\frac{\mathcal{S}(\theta_j, \gamma)}{\mathcal{B}(\theta_j)} \right] + 1 - \frac{n_s}{N} \right) \right) \quad (1.37)$$

$$TS = 2 \sum_j^N \log \left(\frac{n_s}{N} \left[\frac{\mathcal{S}(\theta_j, \gamma)}{\mathcal{B}(\theta_j)} - 1 \right] + 1 \right) \quad (1.38)$$

Equation 1.38 is faster to evaluate, because it bypasses the need to calculate both signal and background energy proxy PDFs explicitly. Instead, we can pre-computing the ratio $\frac{\mathcal{S}}{\mathcal{B}}$ for a variety of spectral indices, saving a per-event division calculation.

An additional simplifying assumption is that neutrinos are typically localised to a resolution of ~ 1 degree, so events which lie many degrees from a source have a negligible probability of being signal. For events lying outside a ± 5 degree box, and those within a ± 5 degree box but with a spatial likelihood ratio less than 10^{-21} , we make the approximation that $\mathcal{S} \approx 0$ so then $TS \approx 0$. Using the formulation in Equation 1.38, we see we can simply neglect to evaluate the likelihood for these events, without altering the final sum. This box cut thus removes the overwhelming majority of events from the likelihood evaluation step, yielding vast speed improvements while having a negligible impact on the fitting process.



2 Stacking Analyses with IceCube

“ We are all in the gutter, but some of us are looking at the stars ”

Oscar Wilde, *Lady Windermere’s Fan*, 1893

A key component of this thesis is the application of the unbinned likelihood analysis method outlined in Chapter 1 to specific astrophysical objects, to test for correlations indicating neutrino emission. The outcomes of these tests were then analysed in the context of diffuse neutrino flux arising from astrophysical populations, following the framework introduced in Chapter ???. All results are outlined below.

All calculations were performed using the *Flarestack* code, developed by the author. Some results presented were previously published in proceedings written by the author [11].

2.1 Tidal Disruption Events

One novel result of this thesis is a stacking analysis of Tidal Disruption Events (TDEs) (see Chapter ??), the first such experimental search for a TDE-neutrino correlation. The details of this analysis are outlined below.

Signal Hypothesis

As outlined Chapter ??, theoretical modelling of neutrino emission in TDEs generally distinguishes between those with relativistic jets and

2.1 Tidal Disruption Events	25
2.2 AT2018cow and FBOTs	33
2.3 Robustness of Limits	35

[11]: Stein (2019), “Search for High-Energy Neutrinos from Populations of Optical Transients”

those without. In recognition of this, we ultimately have two distinct hypotheses to test:

1. Neutrino emission from on-axis relativistic jets
2. Neutrino emission from other mechanisms

The timescales predicted for neutrino emission have varied substantially. In general, neutrino emission is expected to occur close to the peak EM brightness of the flare, with durations of a few hours to ~ 100 days. There are no scenarios for neutrino emission preceding disruption.

Catalogue Compilation

[12]: Auchettl et al. (2017), “New Physical Insights about Tidal Disruption Events from a Comprehensive Observational Inventory at X-Ray Wavelengths”

To perform a correlation analysis, a list of sources must first be compiled. One list of TDEs is maintained by the *OpenTDECatalog* [12], containing relevant metadata and photometry. The database prioritises completeness by containing all objects with a possible TDE classification, even when those classifications are ambiguous [12], and will thus by construction suffer from source contamination. The database itself is maintained by volunteers, and is thus not entirely complete. For the compilation of a catalogue for this thesis, the list from the *OpenTDECatalog* was supplemented by additional objects and data from the literature.

At the time of catalogue compilation in 2018, this database contained approximately 70 objects. Of these, 3 had clear evidence of on-axis relativistic jets, while the remaining 67 did not. We further exclude those objects with peaks >100 days before the start of data-taking during the IC40 data season on 4th May 2008 (see Chapter ??), as these objects did not overlap our neutrino dataset. We are left with 53 TDEs for correlation.

From the starting point of all TDEs, one distinct subsample was created:

- **Jetted TDEs** are X-Ray-bright TDEs which launched relativistic jets pointing towards the Earth. There are three jetted TDEs, and neutrino emission is most promising from this category

These three jetted TDEs share similar properties, namely that they were all sufficiently bright to be discovered serendipitously by observations of the *Swift*-BAT X-ray telescope. They each have well-sampled lightcurves, with the time of jet-launching constrained to a window of a few days. Given the consistent observational features of luminous, hard X-ray emission which rapidly fades, it is likely that all three objects are indeed jetted TDEs. The jetted TDEs were used to test Hypothesis 1.

Hypothesis 2 could then be tested with the remaining “non-jetted” TDEs, defined as those TDEs without on-axis relativistic jets. These non-jetted TDEs form an observationally-distinct class of objects. They may have off-axis relativistic jets, or mildly relativistic outflows, but none exhibit the characteristic hard X-ray emission associated with on-axis relativistic jets .

Beyond this, the properties of non-jetted TDEs are highly heterogeneous. They are discovered across a range of wavelengths (e.g X-ray, Optical, IR)

Table 2.1: Summary of the four TDE catalogues..

Catalogue	Source Class	Size	Description
Jetted	Jetted TDEs	3	<i>Probable TDEs with on-axis jets</i>
Golden	Non-Jetted TDEs	13	<i>Probable TDEs with convincing classification</i>
Silver	Non-Jetted TDEs	24	<i>Candidate TDEs with ambiguous classification</i>
Obscured	Non-Jetted TDEs	13	<i>Candidate TDEs in dusty galaxies</i>

with varying multi-wavelength coverage. There are a handful of compelling TDE candidates, often with comprehensive multi-epoch spectroscopic observations, for which alternative explanations are disfavoured. However, in the vast majority of cases, a definite classification cannot be made. To avoid contamination from misclassified objects, primarily AGN or SN, we define a clean "golden sample" consisting solely of reliably-classified TDEs:

- ▶ **Golden TDEs** are strong candidates where the TDE interpretation is supported by multiple spectra

The remaining objects are then candidate TDEs, with a possible but not definitive classification.

There is one distinct subclass of candidates containing flares observed in dusty galaxies via IR emission [13]. One possible explanation is that the flares arise from a dust-obscured TDE, with the dust then slowly reprocessing the electromagnetic radiation from the galaxy core. For such reprocessing, there would be a time delay between the disruption itself and the corresponding IR flare. Because we expect that neutrinos should begin soon after disruption, the timescale for neutrino emission from obscured TDEs would have significant additional uncertainty.

We thus treat these candidate *obscured TDEs* separately from the other candidate TDEs:

- ▶ **Obscured TDEs** are TDE candidates which occur in very dusty galaxies, and are only observed via reprocessed infra-red emission.
- ▶ **Silver TDEs** are all other candidates, where a TDE interpretation is either likely or not disfavoured.

All catalogues are summarised in Table 2.1, with full details provided in the Appendix (Chapter A).

[13]: Wang et al. (2018), "Long-Term Decline of the Mid-Infrared Emission of Normal Galaxies: Dust Echo of Tidal Disruption Flare?"

Search Windows

To account for the heterogeneous datasets, an individual search window was defined for each TDE, with the aim for identifying the period of peak electromagnetic emission. For jetted/gold/silver TDE, the following criteria were used:

- ▶ For TDEs in which the light curve was observed when rising, the first detection is taken as the window start.
- ▶ For TDEs without an observation during lightcurve rise, the last upper limit is taken as the window start.
- ▶ The maximum date was taken as the date on which the brightest TDE luminosity measurement was performed.

Table 2.2: Summary of results for the four TDE catalogues. For each, an independent stacking analysis was performed. The catalogues covered sources from May 2008 to October 2017, matching the IceCube data-taking period.

Catalogue	Source Class	Size	n_s	γ	TS	Pre-trial p-value
Jetted	Jetted	3	1.5	4.0	0.8	0.40
Golden	Non-Jetted	13	3.9	2.4	2.4	1.00
Silver	Non-Jetted	24	15.6	2.7	7.9	1.00
Obscured	Non-Jetted	13	29.4	2.8	14.8	0.04

- ▶ The window extends from the defined window start to 100 days after the maximum date

Applying these criteria gives a tailored search window for each TDE. Obscured TDEs instead had a search window extending from 300 days before peak to 100 days after peak, to account for potential delay following neutrino emission. The search window for each source is provided in Appendix Chapter A. It is the first such catalogue to contain time windows, and could also be used for stacking analyses of e.g gamma-ray emission.

Analysis and Results

As outlined in Chapter 1, a standard *stacking analysis* requires an additional assumption on the expected relative neutrino emission of each source in a catalogue. However, these TDE catalogues are characterised by small numbers of heterogeneous sources. With a mix of observation cadences and multi-wavelength coverage, there is no obvious proxy for neutrino emission. A common standard-candle approximation, in which each source has the same intrinsic luminosity, is also not well-motivated. There is no evidence of standard-candle behaviour in EM wavelengths, so there is no reason to think it would hold for neutrino emission. We are left with no clear method to compare the relative contributions, and for this reason, an agnostic approach is instead applied. Using the method outlined in Section 1.10, we fit the contribution of each source in the catalogue individually, requiring only that they share a common neutrino spectrum.

Following the procedure in Chapter 1, we perform an unbinned likelihood analysis to obtain results for each catalogue, with fit parameters TS, γ and a number of signal events for each source (n_k). We also obtain a final Test Statistic (TS) value, and calculate a p-value for this TS using pseudotrials. Table 2.2 summarises the results for each catalogue, including $n_s = \sum n_k$. The individual n_k values are provided in the Appendix Chapter A.

There was no significant correlation identified for any of the catalogues. While the Obscured TDE catalogue yielded the most significant pre-trial p-value, after trial correction using Equation 1.18 this is reduced to a value of $p_{\text{post-trial}}=0.15$, and is thus consistent with background expectations. No discovery of neutrino emission from TDEs is claimed, and *we do not reject the null hypothesis that TDEs and neutrinos are uncorrelated*.

Catalogue limits

Being unable to reject the null hypothesis, we can instead set an upper limit on neutrino emission, by ruling out scenarios for which we would have expected to reject the null hypothesis. We follow the procedure outlined in Section 1.6 to set an upper limit, at 90% confidence, using pseudoexperiments with simulated signal. In common with most IceCube studies, these limits are only valid *under the assumption that the signal looks like the baseline IceCube MC*, and thus that *the impact of all systematic effects are negligible*.

While our search results in Table 2.2 are agnostic to the relative neutrino contribution of each source, any pseudoexperiments involving simulated signal must make an assumption regarding the intrinsic neutrino luminosity of each source. Though it remains a poor approximation for EM emission, we inject neutrinos under *the assumption that each catalogue source emits the same number of neutrinos according to the same intrinsic energy spectrum*, i.e that TDEs are neutrino standard candles. The corresponding flux on Earth is thus proportional to the inverse distance squared of each source. This flux is injected uniformly across the search windows for each source, as defined in Appendix (Chapter A). To conserve energy, and the flux-per-source is then inversely proportional to the length of the search window.

All limits derived below are only valid in the case that all of these assumptions are true. Upper limits are derived for combined neutrino+anti-neutrino emission under the *assumption of an unbroken neutrino power law, between 100 GeV and 10 PeV*, for a variety of spectral limits. These upper limits are shown in Figure 2.1, in units of integrated neutrino+anti-neutrino fluence for the entire catalogue.

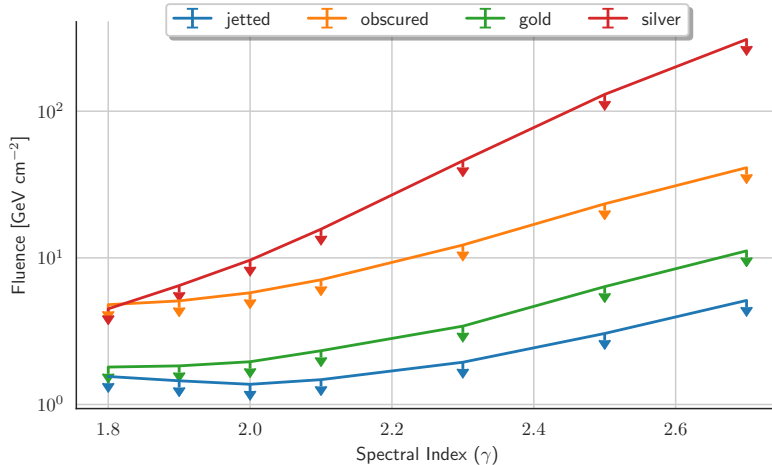


Figure 2.1: Limits on the neutrino fluence for each catalogue.

If Figure 2.1 is contrasted with the time-integrated point source sensitivity (seen in Figure 1.17), it is clear that the upper limits are substantially higher than the sensitivity for a single source in ten years of data. This is however expected, as a consequence of the additional background that comes with stacking multiple sources. The limits are ranked in order of ascending catalogue size, with the 3-source jettled catalogue being the most stringent and the 24-source silver catalogue being the weakest. The

obscured catalogue has a somewhat weaker limit than expected, in notable contrast to the equally-sized gold catalogue, because the former demonstrated a relatively large neutrino excess.

We can convert these to limits on the integrated neutrino+anti-neutrino per-flavour energy for each source, as shown in Figure 2.2. There is substantially more variation in the scale of these limits, driven by the typical distance scale of the nearest sources in each catalogue (see Appendix Chapter A). For the Jetted TDEs, the nearest source lies at ~ 2000 Mpc, while for silver catalogue the nearest source lies at ~ 2 Mpc, explaining the dramatic variation in limits between catalogues. All these intrinsic energies are presented as *isotropic-equivalent*, and thus quoted assuming that the emission is emitted isotropically. This is of particular relevance for the Jetted TDEs, for which emission is likely to be highly beamed. As the exact beaming angle is unclear, it is conventional to present such isotropic-equivalent values for comparison, with the true energy likely to be somewhat lower.

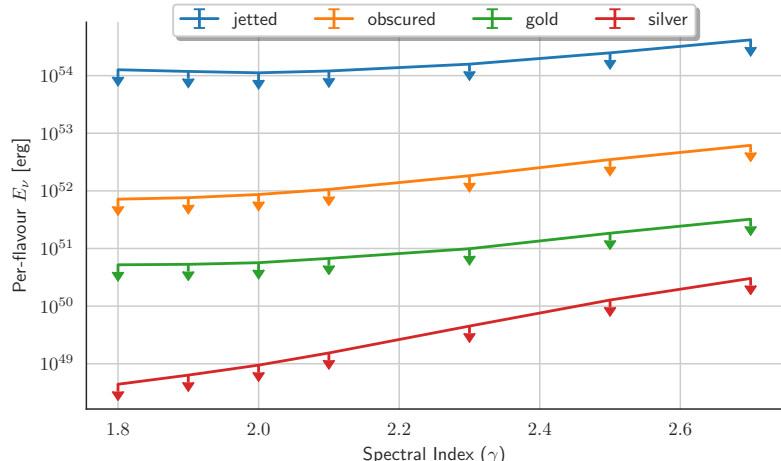


Figure 2.2: Limits on the per-source neutrino emission for each catalogue.

Population limits

While the limits presented above constrain the contribution of those catalogues tested, we ultimately wish to constrain neutrino emission for the TDE population as a whole. If we *assume that catalogue sources are representative of the broader population*, we can extrapolate from our per-source standard candle limits in Figure 2.2 to the population flux. We seek to constrain the flux of two populations, namely jetted and non-jetted TDEs. For the latter case, we rely on the results of the golden TDE catalogue, since the extrapolation *implicitly requires that the catalogues are not contaminated by misclassified objects*.

Using the most recent IceCube global fit of the astrophysical neutrino flux [14], with a best-fit spectrum of $E^{-2.50}$, we follow the procedure outline in Chapter ???. We combine the golden TDE per-source limit shown in Figure 2.2, with a central local rate of 8×10^{-7} Mpc $^{-3}$ year $^{-1}$ [15] and a TDE source evolution [16] parameterised as:

[14]: Aartsen et al. (2015), “A Combined Maximum-likelihood Analysis of the High-energy Astrophysical Neutrino Flux Measured with IceCube”

[15]: van Velzen (2018), “On the Mass and Luminosity Functions of Tidal Disruption Flares: Rate Suppression due to Black Hole Event Horizons”

[16]: Sun et al. (2015), “Extragalactic High-energy Transients: Event Rate Densities and Luminosity Functions”

$$\rho(z) \propto \left((1+z)^{-0.4} + \left(\frac{1+z}{1.43} \right)^{6.4} + \left(\frac{1+z}{2.66} \right)^{14} \right)^{-\frac{1}{2}} \quad (2.1)$$

With this evolution, we constrain the contribution of non-jetted TDEs to be less than 25.3% of the total. For jetted TDEs, under the assumption that they follow the same underlying source evolution in Equation 2.1 with a central rate of $3 \times 10^{-11} \text{ Mpc}^{-3} \text{ year}^{-1}$ [16], we find that they must contribute less than 1.3% of the total. These constraints are illustrated in Figure 2.3.

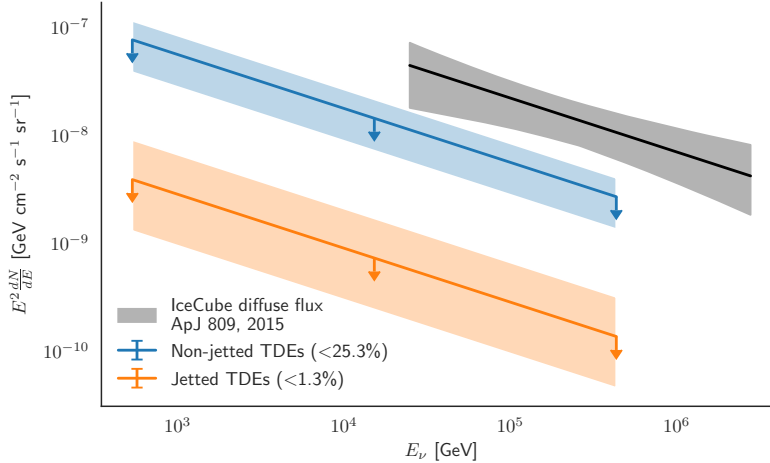


Figure 2.3: Limits on the contribution of jetted and non-jetted TDEs to the diffuse neutrino flux.

As the contribution from a population is directly proportional to the local population rate, the shaded bands indicate the uncertainty in our limits arising from rate estimates. For TDEs, these rates are a large source of uncertainty in neutrino flux. It will require systematic evaluation of observed TDE rates to enable more precise limits on neutrino emission. Any refined rate estimate can be used to linearly rescale these limits. Propagating through the current local rate uncertainty, we constrain non-jetted TDEs to be less than 12.7% - 38.0%, and jetted TDEs to be less than 0.4% - 3.0% of the total. With a more precise future measurement of the local TDE rate, these values can be linearly rescaled to provide more accurate limits.

Such limits also critically depend on the source evolution of TDEs as a function of redshift, but this is not strongly constrained observationally because TDEs detections are generally confined to the local universe ($z \lesssim 0.3$). Estimates are made primarily based on theoretical predictions derived from the rate of supermassive black holes (see Chapter ??) [16]. We can instead consider a source evolution similar to the Star Formation Rate (SFR) [17], parameterised as:

$$\rho(z) \propto \frac{(1+z)^{2.7}}{1 + ((1+z)/2.9)^{5.6}} \quad (2.2)$$

[17]: Madau et al. (2014), “Cosmic Star-Formation History”

With Equation 2.2, we would then find limits of 108.3% (54.2% - 162.5%) for non-jetted TDEs and 5.5 % (1.8% - 12.8%) for jetted TDEs. These limits are shown in Figure 2.4. For such a scenario, the contribution of unresolved non-jetted TDEs is so large that the measured flux itself

Table 2.3: Summary of the five individual TDEs for which the temporal-cluster-search method was applied. All but AT2018cow were included in the stacking analysis.

Source	R.A (deg.)	Dec (deg.)	T ₀ (MJD)	T ₁ (MJD)	n _s	γ	t _s (MJD)	t _e (MJD)	TS
Swift J1644+57	251.21	57.58	55644.00	55749.00	0.68	1.98	55650.90	55746.25	0.06
Swift J2058+05	314.58	5.23	55694.00	55798.00	2.78	4.00	55774.25	55780.00	2.28
ASASSN-14li	192.06	17.77	56851.00	57072.00	2.95	2.53	57022.68	57032.75	1.52
XMMSL1 J0740-85	115.03	85.66	56718.00	56848.00	2.84	2.19	56806.95	56807.51	3.49
AT2018cow	244.00	22.27	58256.90	58386.90	5.91	2.98	58283.83	58298.53	3.91

provides a stricter constraint than the catalogue test. However, even in that extreme scenario, the contribution of jetted TDEs to the diffuse neutrino flux remains subdominant.

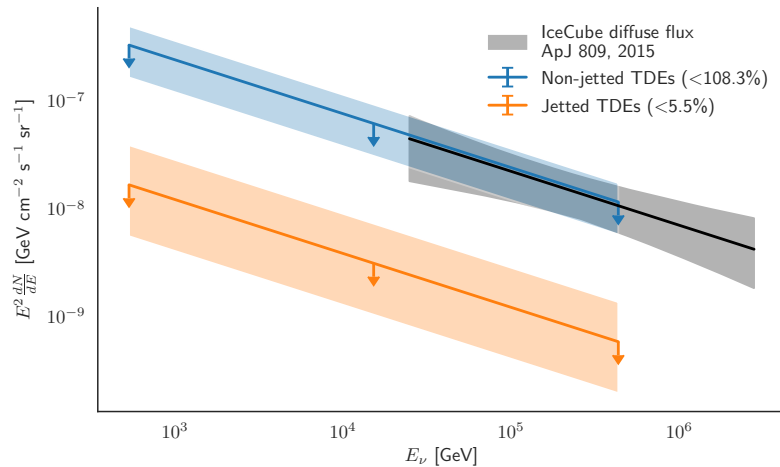


Figure 2.4: Limits on the contribution of jetted and non-jetted TDEs to the diffuse neutrino flux, under the assumption of a source evolution proportional to the Star Formation Rate.

Individual TDEs

In addition to the stacking analysis, four TDEs were selected for individual analysis. Two of the three jetted TDEs, Swift J1644+57 and Swift J2058+05, were chosen due to their luminosity, as well as their position in the northern hemisphere where IceCube has the highest effective area. In addition, ASSASN-14li and XMMSL1 J0740-85 were chosen as non-jetted TDEs which were both nearby and bright. These four TDEs were the only catalogue sources that were also detected in radio observations, typically a tracer for relativistic particle acceleration. For each of the four individual TDEs, searches were conducted for neutrino clustering in both time and space, following the procedure outlined in Section 1.9. All single-object tests are described in Table 2.3.

The results of each fit are provided in Table 2.3, alongside pre-trial p-values. No significant emission was identified, and no discovery is claimed. Instead, upper limits are derived on neutrino emission for each source. As described in Section 1.9, the cluster-search method is more sensitive to shorter-scale emission. Upper limits were derived under the conservative assumption that neutrino emission was distributed uniformly in the search window, with any emission on shorter timescales being more constrained.

2.2 AT2018cow and FBOTs

Following the four stacking analyses and four cluster-search analyses described above, an additional analysis was later performed on AT2018cow [18], a transient first discovered in 2018. It is now thought that AT2018cow was a nearby example of the recently-identified population known as “Fast Blue Optical Transients” (FBOTs) introduced in Chapter ??.

However, at the time of discovery, AT2018cow was initially thought to be a bright Broad-Lined type Ic (Ic-BL) supernova, and thus a member of the rare subclass associated with long GRBs and relativistic jets [19]. As outlined in Chapter ??, many models predict that such SNe may be neutrino sources, so an IceCube *Fast Response Analysis* was run on AT2018cow shortly after discovery [20]. The IceCube search targeted choked-jet neutrino emission, and thus covered the 3-day period from the last non-detection to the first detection, aiming to isolate the supernova explosion time at which the neutrino emission would be expected. Ultimately, an excess of neutrinos was found in this time period, with a significance of 1.8σ [21]. The excess itself consisted of two signal-like neutrinos, which were considered significant owing to the small expected background for such a short search window.

Later multi-wavelength observations of AT2018cow were not consistent with a traditional Ic-BL SN, and the transient was later identified as a nearby example of an FBOT [22]. The exact nature of these FBOTs had been difficult to probe, since they were primarily discovered at high redshift [23], but promptly-identified AT2018cow at 60 Mpc provided a rich multi-wavelength dataset. It has since variously interpreted as a TDE with an Intermediate-Mass Black Hole, an extreme supernova or a Magnetar. In light of these developments, AT2018cow was re-analysed by the author in the context of a potential TDE classification. As for the other four individual TDEs detailed above, a dedicated search for neutrino clustering on timescales up to 130 days, extending from 30 days before peak to 100 days afterwards, was undertaken. For this purpose, an additional year of IceCube data extending to October 2018 was analysed.

In this analysis of AT2018cow, a small excess was again found. Although the best-fit cluster from this search included the two signal-like neutrinos from the original IceCube analysis, when accounting for the expected fluctuations arising from background over the much longer 130 day search window, the significance of the excess was just 0.5σ . The result is thus entirely consistent with expectations from atmospheric background, while not contradicting the original result published at the time. As such, no discovery is claimed and upper limits for AT2018cow are accordingly derived (illustrated in Figure 2.5). Though AT2018cow was not included in the catalogues when the stacking analysis was performed, it would naturally belong to the silver non-jetted TDE sample.

The analysis of AT2018cow is the first example of a test for neutrino emission from FBOTs. In the time since discovery in 2018, there have been theoretical studies considering possible neutrino emission from FBOTs in general, and AT2018cow in particular [24]. The predicted neutrino emission is typically several orders of magnitude below the limits presented

[18]: Margutti et al. (2019), “An Embedded X-Ray Source Shines through the Aspherical AT 2018cow: Revealing the Inner Workings of the Most Luminous Fast-evolving Optical Transients”

[19]: Woosley et al. (2006), “The Supernova Gamma-Ray Burst Connection”

[20]: Abbasi et al. (2020), “Follow-up of astrophysical transients in real time with the IceCube Neutrino Observatory”

[21]: Blaufuss (2018), “AT2018cow: IceCube neutrino search”

[22]: Perley et al. (2019), “The Fast, Luminous Ultraviolet Transient AT2018cow: Extreme Supernova, or Disruption of a Star by an Intermediate-Mass Black Hole?”

[23]: Drout et al. (2014), “Rapidly Evolving and Luminous Transients from Pan-STARRS1”

[24]: Fang et al. (2019), “Multimessenger Implications of AT2018cow: High-energy Cosmic-Ray and Neutrino Emissions from Magnetar-powered Superluminous Transients”

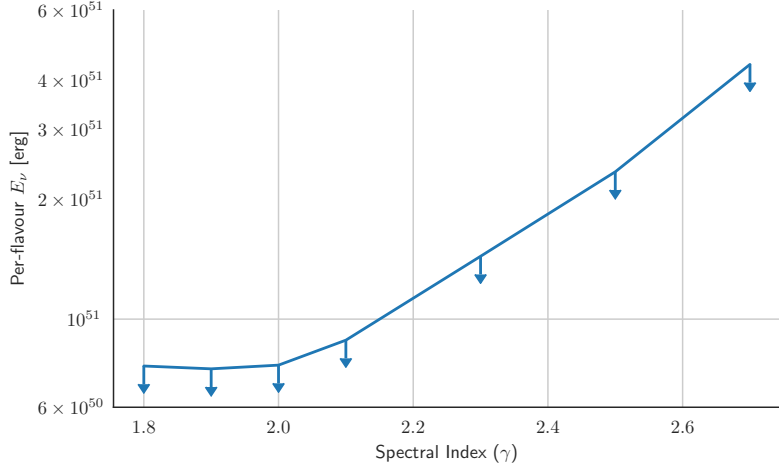
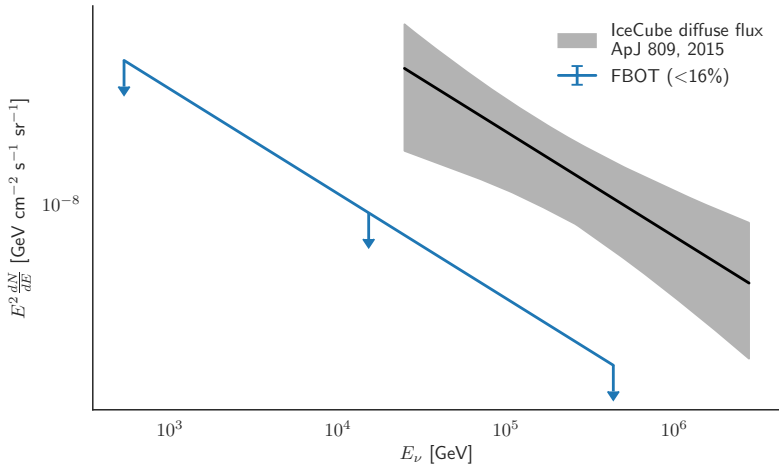


Figure 2.5: Limits on neutrino emission from AT2018cow, as a function of spectral index.

in Figure 2.5, and thus further supports the likely atmospheric origin for the neutrino excess [21].

However, given that AT2018cow is by far the closest example of an FBOT, we can already consider the implications for the broader FBOT population emission. While initial estimates suggested that these objects might equal \sim 4-7% of the CCSN rate [23, 24], these estimates have been superseded by results from magnitude-limited surveys such as ZTF, where a lack of additional FBOTs strongly suggest that the local rate must be \sim 0.1% of the CCSN rate [ADD CITATION WHEN ZTF FBOT PAPER IS OUT IN MAY]

Following the same procedure for TDEs, we find that FBOTs contribute less than 16% of the total diffuse neutrino flux *assuming that AT2018cow is representative of the broader FBOT population*. This further assumes a CCSN-like source evolution [17], proportional to the star formation rate, and a local FBOT rate of $4 \times 10^{-7} \text{ Mpc}^{-3} \text{ yr}^{-1}$ [25]. These limits are agnostic to the exact nature of FBOTs, whether they are a distinct population or a rare subgroup of some broader object class. In any case, it is clear that any contribution of FBOTs to the diffuse neutrino flux must be subdominant.



[17]: Madau et al. (2014), “Cosmic Star-Formation History”

Figure 2.6: Limits on neutrino emission from FBOTs, using the limits from AT2018cow under the assumption of neutrino standard candles.

2.3 Robustness of Limits

One key additional point is how robust the derived constraints are, given the many stated caveats. Full systematic studies are not typically re-performed for each individual IceCube neutrino source analysis [4]. This is due primarily to evidence from previous studies which demonstrated that the impact of systematic uncertainties on a typical Icecube neutrino point source search is $O(\sim 10\%)$, dominated by uncertainty on ice optical properties and DOM performance [26]. This value is completely negligible in comparison to uncertainties on astrophysical population rates, as well as to additional uncertainties on the relative distribution of neutrinos across an astrophysical population.

The searches introduced above are time-dependent analyses performed on specific windows, and are thus completely insensitive to any neutrino emission which may fall outside these windows. However, while the duration of neutrino emission may be uncertain for transients, it is expected that at least some substantial fraction of neutrino emission should occur during the periods of peak electromagnetic brightness. Thus the limits derived above can be extrapolated to cover neutrino emission models extending beyond the tested period. For example, if one predicts that only 50% of neutrino emission from Jetted TDEs would occur in the first 100 days, the population limit would be twice as high (2.6% rather than 1.3%) but still constraining.

A similar argument can be applied for deviations from an unbroken neutrino power law. For TDEs this would not be surprising, because the ρ_γ neutrino production models introduced in Chapter ?? would instead favour a peaked neutrino spectrum. However, while the energy weightings illustrated in Figure 1.7 are based on different power laws, the likelihood analysis will detect excesses from any neutrino spectrum. If the signal follows the same energy distribution of the background, the energy term in the Point Source Likelihood (Equation 1.17) will provide no discriminating power, but the analysis can still identify the corresponding spatial clustering. If however there is an additional excess of neutrinos at either high or low energies, that can be well-approximated by a hard or soft neutrino power law respectively. Given that discoveries can be made with just 10-20 neutrinos, there is little power to constrain exact spectral shapes.

However, as can be seen in Figure 2.1, the strength of the constraint depends on the general energy range at which neutrino emission is expected. This can be seen even more clearly in Figure 2.7, where the sensitivity is illustrated as a function of true neutrino energy. For a source at the horizon ($\sin(\delta) = 0.0$), in the range >10 TeV, the sensitivity does not vary by much, but is substantially worse at lower energies. For a more northern source ($\sin(\delta) = 0.5$), the sensitivity is similarly stable in the range ~ 10 TeV - 1 PeV, above which it begins to degrade because of Earth absorption. This behaviour is in contrast to sources in the southern sky, for which the analysis is much less sensitive but improves with increasing energy. Within each tested catalogues, at least one of the five nearest sources lies at the horizon, and limits are generally dominated by such sources. We can thus state that all neutrinos emission scenarios between ~ 10 TeV and ~ 1 PeV will be somewhat constrained by these

[4]: Aartsen et al. (2020), “Time-Integrated Neutrino Source Searches with 10 Years of IceCube Data”

[26]: Aartsen et al. (2017), “All-sky Search for Time-integrated Neutrino Emission from Astrophysical Sources with 7 yr of IceCube Data”

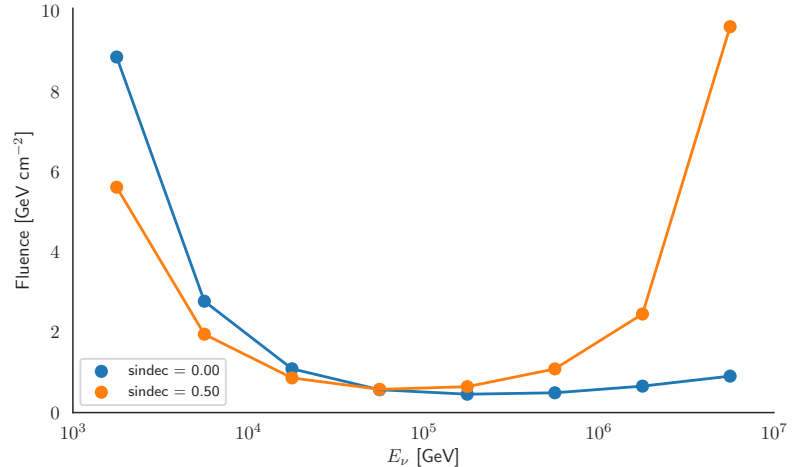


Figure 2.7: Sensitivity of the Point Source Likelihood for a point source as a function of energy.

results regardless of the exact energy spectrum, though clearly will be different for each individual model.

As was demonstrated for both TDEs and FBOTs, uncertainty on the properties of a given astrophysical population remains an important source of uncertainty in constraining the overall population neutrino emission. The local rate itself remains challenging to constrain particularly for rare transient classes such as jetted TDEs or FBOTs, though wide-field time-domain surveys such as ZTF and LSST should lead to continuing improvements in precision. Constraining the rate evolution is more challenging, particularly because even deep surveys such as LSST will not probe transient rates at very high redshift where much of the neutrino emission is expected. Ultimately this source of uncertainty will likely continue to dominate limits even with next-generation neutrino detectors and transient surveys.

OPTICAL FOLLOW-UP WITH ZTF

CONCLUSION

APPENDIX

A

TDE Catalogue Results

Table A.1: Summary of the Jetted TDE catalogue.

Source	R.A (deg.)	Dec (deg.)	Distance (Mpc)	T ₀ (MJD)	T ₁ (MJD)	n _s
Swift J1644+57	251.21	57.58	1909	55644	55749	0.00
Swift J1112-82	167.95	-82.65	5821	55724	55828	0.00
Swift J2058+05	314.58	5.23	8308	55694	55798	1.51

Table A.2: Summary of the Golden TDE catalogue.

Source	R.A (deg.)	Dec (deg.)	Distance (Mpc)	T_0 (MJD)	T_1 (MJD)	n_s
iPTF16fnl	7.49	32.89	72	57600	57730	0.00
XMMSL1 J0740-85	115.03	85.66	76	56718	56848	0.00
ASASSN-15oi	309.79	-30.76	88	57228	57359	0.00
ASASSN-14li	192.06	17.77	91	56851	57072	0.00
ASASSN-14ae	167.17	34.10	195	56658	56851	3.40
PTF09ge	224.26	49.61	290	54953	55083	0.00
iPTF16axa	255.89	30.59	505	57432	57651	0.00
PTF09axc	223.30	22.24	538	55002	55135	0.00
PTF10nuj	246.60	54.71	627	55343	55473	0.47
PS1-10jh	242.37	53.67	826	55326	55470	0.00
PTF09djl	248.48	30.24	904	55020	55150	0.00
PTF11qlr	253.53	41.34	1031	55721	55860	0.00
PS1-11af	149.36	3.23	2232	55560	55690	0.00

Table A.3: Summary of the Silver TDE catalogue.

Source	R.A (deg.)	Dec (deg.)	Distance (Mpc)	T_0 (MJD)	T_1 (MJD)	n_s
NGC 247	11.79	-20.76	2	55593	57070	0.00
UGC 03317	83.41	73.72	18	55096	55568	0.00
PGC 1185375	225.96	1.13	23	55228	55358	0.00
PGC 1190358	226.37	1.29	33	55194	55363	0.00
PGC 015259	67.34	-4.76	64	55215	55345	1.48
AT2016ezh	29.52	-0.87	367	57597	57753	0.00
J233454	353.73	14.95	500	55129	55319	1.55
OGLE17aaaj	29.10	-71.07	546	57393	57858	0.00
F01004-2237	15.71	-22.37	555	55219	55528	0.00
J094608	146.54	35.21	561	55679	55834	3.51
XJ1500+0154	225.22	1.91	695	54509	54974	0.00
SDSSJ1201	180.40	30.05	700	54992	55457	0.00
CSS100217	157.30	40.71	705	55183	55350	0.00
SN2017bcc	172.97	30.00	711	57802	57938	0.00
DES14C1kia	53.70	-26.33	785	56972	57121	0.32
OGLE16aaa	16.84	-64.27	804	57373	57506	0.00
D23H-1	353.00	0.29	912	54342	54472	1.00
Dougie	182.20	43.02	942	54832	54962	0.00
PS1-10adi	310.69	15.51	1008	55391	55542	0.00
J094806	147.03	3.30	1031	54864	55079	0.57
PTF10iya	219.67	37.66	1127	55323	55453	0.00
ASASSN-15lh	330.56	-61.66	1175	57148	57278	0.00
PS1-13jw	131.22	42.96	1850	56323	56458	0.52
PS1-12yp	202.98	23.90	3447	55933	56126	6.65

Table A.4: Summary of the Obscured TDE catalogue.

Source	R.A (deg.)	Dec (deg.)	Distance (Mpc)	T ₀ (MJD)	T ₁ (MJD)	n _s
J130819	197.08	43.76	162	54991	55456	7.10
J134244	205.69	5.52	162	54845	55310	0.65
J100933	152.39	23.38	328	54962	55427	0.00
J133737	204.40	20.40	331	54839	55304	0.00
J121116	182.82	0.23	349	54999	55464	0.00
J142401	216.01	29.84	394	54845	55310	0.00
J030257	45.74	-8.50	493	54857	55322	0.00
J141036	212.65	26.91	501	55206	55671	4.87
J113527	173.86	39.47	507	54974	55439	0.00
J145851	224.72	17.85	548	54857	55322	11.88
J133837	204.66	57.52	601	54983	55448	1.39
J155223	238.10	32.58	605	55045	55510	0.63
J091225	138.10	6.17	697	54955	55420	1.09
J123715	189.31	60.20	1083	54967	55432	1.74

Bibliography

Here are the references in citation order.

- [1] Robert Stein et al. *icecube/flarestack*. Apr. 2020. doi: [10.5281/zenodo.3619383](https://doi.org/10.5281/zenodo.3619383) (cited on page 6).
- [2] M. G. Aartsen et al. “The IceCube Neutrino Observatory: Instrumentation and Online Systems.” In: *JINST* 12.03 (2017), P03012. doi: [10.1088/1748-0221/12/03/P03012](https://doi.org/10.1088/1748-0221/12/03/P03012) (cited on page 7).
- [3] IceCube Collaboration et al. “Search for steady point-like sources in the astrophysical muon neutrino flux with 8 years of IceCube data.” In: *arXiv e-prints*, arXiv:1811.07979 (Nov. 2018), arXiv:1811.07979 (cited on page 7).
- [4] M. G. Aartsen et al. “Time-Integrated Neutrino Source Searches with 10 Years of IceCube Data.” In: *Phys. Rev. Lett.* 124.5, 051103 (Feb. 2020), p. 051103. doi: [10.1103/PhysRevLett.124.051103](https://doi.org/10.1103/PhysRevLett.124.051103) (cited on pages 7, 35).
- [5] Patrick Heix et al. “Seasonal Variation of Atmospheric Neutrinos in IceCube.” In: *arXiv e-prints*, arXiv:1909.02036 (Sept. 2019), arXiv:1909.02036 (cited on page 8).
- [6] D. Chirkov and M. Rongen. “Light diffusion in birefringent polycrystals and the IceCube ice anisotropy.” In: *36th International Cosmic Ray Conference (ICRC2019)*. Vol. 36. International Cosmic Ray Conference. July 2019, 854, p. 854 (cited on page 9).
- [7] J. Neyman and E. S. Pearson. “On the Problem of the Most Efficient Tests of Statistical Hypotheses.” In: *Philosophical Transactions of the Royal Society of London Series A* 231 (Jan. 1933), pp. 289–337. doi: [10.1098/rsta.1933.0009](https://doi.org/10.1098/rsta.1933.0009) (cited on page 14).
- [8] Jim Braun et al. “Methods for point source analysis in high energy neutrino telescopes.” In: *Astroparticle Physics* 29.4 (May 2008), pp. 299–305. doi: [10.1016/j.astropartphys.2008.02.007](https://doi.org/10.1016/j.astropartphys.2008.02.007) (cited on page 14).
- [9] S.S. Wilks. “The Large-Sample Distribution of the Likelihood Ratio for Testing Composite Hypotheses.” In: *Annals Math. Statist.* 9.1 (1938), pp. 60–62. doi: [10.1214/aoms/1177732360](https://doi.org/10.1214/aoms/1177732360) (cited on page 15).
- [10] Alexander Johannes Stasik. “Search for High Energetic Neutrinos from Core Collapse Supernovae using the IceCube Neutrino Telescope.” PhD thesis. Humboldt U., Berlin, 2017. doi: [10.18452/18729](https://doi.org/10.18452/18729) (cited on page 22).
- [11] R. Stein. “Search for High-Energy Neutrinos from Populations of Optical Transients.” In: *36th International Cosmic Ray Conference (ICRC2019)*. Vol. 36. International Cosmic Ray Conference. July 2019, 1016, p. 1016 (cited on page 25).
- [12] Katie Auchettl, James Guillochon, and Enrico Ramirez-Ruiz. “New Physical Insights about Tidal Disruption Events from a Comprehensive Observational Inventory at X-Ray Wavelengths.” In: *ApJ* 838.2, 149 (Apr. 2017), p. 149. doi: [10.3847/1538-4357/aa633b](https://doi.org/10.3847/1538-4357/aa633b) (cited on page 26).
- [13] Tinggui Wang et al. “Long-Term Decline of the Mid-Infrared Emission of Normal Galaxies: Dust Echo of Tidal Disruption Flare?” In: *Mon. Not. Roy. Astron. Soc.* 477.3 (2018), pp. 2943–2965. doi: [10.1093/mnras/sty465](https://doi.org/10.1093/mnras/sty465) (cited on page 27).
- [14] M. G. Aartsen et al. “A Combined Maximum-likelihood Analysis of the High-energy Astrophysical Neutrino Flux Measured with IceCube.” In: *ApJ* 809.1, 98 (Aug. 2015), p. 98. doi: [10.1088/0004-637X/809/1/98](https://doi.org/10.1088/0004-637X/809/1/98) (cited on page 30).
- [15] S. van Velzen. “On the Mass and Luminosity Functions of Tidal Disruption Flares: Rate Suppression due to Black Hole Event Horizons.” In: *ApJ* 852.2, 72 (Jan. 2018), p. 72. doi: [10.3847/1538-4357/aa998e](https://doi.org/10.3847/1538-4357/aa998e) (cited on page 30).

- [16] Hui Sun, Bing Zhang, and Zhuo Li. “Extragalactic High-energy Transients: Event Rate Densities and Luminosity Functions.” In: *Astrophys. J.* 812.1 (2015), p. 33. doi: [10.1088/0004-637X/812/1/33](https://doi.org/10.1088/0004-637X/812/1/33) (cited on pages 30, 31).
- [17] Piero Madau and Mark Dickinson. “Cosmic Star-Formation History.” In: *ARA&A* 52 (Aug. 2014), pp. 415–486. doi: [10.1146/annurev-astro-081811-125615](https://doi.org/10.1146/annurev-astro-081811-125615) (cited on pages 31, 34).
- [18] R. Margutti et al. “An Embedded X-Ray Source Shines through the Aspherical AT 2018cow: Revealing the Inner Workings of the Most Luminous Fast-evolving Optical Transients.” In: *Astrophys. J.* 872.1 (2019), p. 18. doi: [10.3847/1538-4357/aaafa01](https://doi.org/10.3847/1538-4357/aaafa01) (cited on page 33).
- [19] S. E. Woosley and J. S. Bloom. “The Supernova Gamma-Ray Burst Connection.” In: *ARA&A* 44.1 (Sept. 2006), pp. 507–556. doi: [10.1146/annurev.astro.43.072103.150558](https://doi.org/10.1146/annurev.astro.43.072103.150558) (cited on page 33).
- [20] R. Abbasi et al. “Follow-up of astrophysical transients in real time with the IceCube Neutrino Observatory.” In: *arXiv e-prints*, arXiv:2012.04577 (Dec. 2020), arXiv:2012.04577 (cited on page 33).
- [21] E. Blaufuss. “AT2018cow: IceCube neutrino search.” In: *The Astronomer’s Telegram* 11785 (June 2018) (cited on pages 33, 34).
- [22] Daniel A. Perley et al. “The Fast, Luminous Ultraviolet Transient AT2018cow: Extreme Supernova, or Disruption of a Star by an Intermediate-Mass Black Hole?” In: *Mon. Not. Roy. Astron. Soc.* 484.1 (2019), pp. 1031–1049. doi: [10.1093/mnras/sty3420](https://doi.org/10.1093/mnras/sty3420) (cited on page 33).
- [23] M. R. Drout et al. “Rapidly Evolving and Luminous Transients from Pan-STARRS1.” In: *ApJ* 794.1, 23 (Oct. 2014), p. 23. doi: [10.1088/0004-637X/794/1/23](https://doi.org/10.1088/0004-637X/794/1/23) (cited on pages 33, 34).
- [24] Ke Fang et al. “Multimessenger Implications of AT2018cow: High-energy Cosmic-Ray and Neutrino Emissions from Magnetar-powered Superluminous Transients.” In: *ApJ* 878.1, 34 (June 2019), p. 34. doi: [10.3847/1538-4357/ab1b72](https://doi.org/10.3847/1538-4357/ab1b72) (cited on pages 33, 34).
- [25] Anna Y. Q. Ho et al. “The Koala: A Fast Blue Optical Transient with Luminous Radio Emission from a Starburst Dwarf Galaxy at $z = 0.27$.” In: *ApJ* 895.1, 49 (May 2020), p. 49. doi: [10.3847/1538-4357/ab8bcf](https://doi.org/10.3847/1538-4357/ab8bcf) (cited on page 34).
- [26] M. G. Aartsen et al. “All-sky Search for Time-integrated Neutrino Emission from Astrophysical Sources with 7 yr of IceCube Data.” In: *ApJ* 835.2, 151 (Feb. 2017), p. 151. doi: [10.3847/1538-4357/835/2/151](https://doi.org/10.3847/1538-4357/835/2/151) (cited on page 35).

Greek Letters with Pronunciations

Character	Name	Character	Name
α	alpha <i>AL-fuh</i>	ν	nu <i>NEW</i>
β	beta <i>BAY-tuh</i>	ξ, Ξ	xi <i>KSIGH</i>
γ, Γ	gamma <i>GAM-muh</i>	\omicron	omicron <i>OM-uh-CRON</i>
δ, Δ	delta <i>DEL-tuh</i>	π, Π	pi <i>PIE</i>
ϵ	epsilon <i>EP-suh-lon</i>	ρ	rho <i>ROW</i>
ζ	zeta <i>ZAY-tuh</i>	σ, Σ	sigma <i>SIG-muh</i>
η	eta <i>AY-tuh</i>	τ	tau <i>TOW (as in cow)</i>
θ, Θ	theta <i>THAY-tuh</i>	v, Y	upsilon <i>OOP-suh-LON</i>
ι	iota <i>eye-OH-tuh</i>	ϕ, Φ	phi <i>FEE, or FI (as in hi)</i>
κ	kappa <i>KAP-uh</i>	χ	chi <i>KI (as in hi)</i>
λ, Λ	lambda <i>LAM-duh</i>	ψ, Ψ	psi <i>SIGH, or PSIGH</i>
μ	mu <i>MEW</i>	ω, Ω	omega <i>oh-MAY-guh</i>

Capitals shown are the ones that differ from Roman capitals.

Alphabetical Index

preface, v